Organic Rankine cycle systems for engine waste-heat recovery: Heat exchanger design in space-constrained applications

Xiaoya Li[1,2], Jian Song[2], Guopeng Yu[3], Youcai Liang[3],

Hua Tian[1], Gequn Shu[1,*], Christos N. Markides[2,+]

[1] State Key Laboratory of Engines, Tianjin University, 92 Weijin Road, Nankai District, Tianjin 300072, China

[2] Clean Energy Processes (CEP) Laboratory, Department of Chemical Engineering, Imperial College London, UK

[3] Systems, Power & Energy Research Division, School of Engineering, University of Glasgow, UK

* Corresponding author. E-mail: sgq@tju.edu.cn

+ Corresponding author. E-mail: c.markides@imperial.ac.uk

Abstract

Organic Rankine cycle (ORC) systems are a promising solution for improving internal combustion engine efficiencies, however, conflicts between the pressure drops in the heat exchangers, overall thermodynamic performance and economic viability are acute in this space-constrained application. This paper focuses on the interaction of the heat exchanger pressure drop (HEPD) and the thermo-economic performance of ORC systems in engine waste-heat recovery applications. An iterative procedure is included in the thermo-economic analysis of such systems that quantifies the HEPD in each case, and uses this information to revise the cycle and to resize the components until convergence. The newly proposed approach is compared with conventional methods in which the heat exchangers are sized after thermodynamic cycle modelling and the pressure drops through them are ignored, in order to understand and quantify the effects of the HEPD on ORC system design and working fluid selection. Results demonstrate that neglecting the HEPD leads to significant overestimations of both the thermodynamic and the economic performance of ORC systems, which for some indicators can be as high as >80% in some cases, and that this can be effectively avoided with the improved approach that accounts for the HEPD. In such space-limited applications, the heat exchangers can be designed with a smaller cross-section in order to achieve a better compromise between packaging volume, heat transfer and ORC net power output. Furthermore, we identify differences in working fluid selection that arise from the fact that different working fluids give rise to different levels of HEPD. The optimized thermo-economic approach proposed here improves the accuracy and reliability of conventional early-stage engineering design and assessments, which can be extended to other similar thermal systems (i.e., CO_2 cycle, Brayton cycle, etc.) that involve heat exchangers integration in similar applications.

Keywords: engine efficiency; heat exchanger design; organic Rankine cycle (ORC); thermo-economic analysis; waste heat; working fluid selection

Nomenclature

A	area (m^2)	bb	bundle to shell clearance
B_i, K_i, C_i	parameters for cost	bc	central baffle spacing
c_p	specific heat capacity (J/kg·K)	boiling	boiling
C_{ann}	annual cost ($)	BM	bare module
C_{elec}	electricity price ($/kWh)	c	condenser; cold fluid side; baffle cut; contraction
C_{in}	initial investment cost ($)	cond	condensation
C_P^0	cost at ambient pressure and using carbon steel	crit	critical
D, d	diameter (m)	desup	de-superheating
F_p	pressure factor	e	evaporator; expander; entrance and exit
F_M	material factor	evap	evaporation
Fr	Froude number	f	working fluid
f_s	friction factor	forced	forced-convective
G	mass flux ($kg/m^2 \cdot s$)	g	exhaust gas
Ga	Galileo number	h	hot fluid side
h	specific enthalpy (J/kg)	in, i	inlet
hr_{full_load}	full-load operation duration (h)	l	leakage; liquid
j, R	correction factors	m	midline; mean
i	interest rate	n	nozzle
K	total heat transfer coefficient ($W/m^2 \cdot K$)	net	net
k	discount rate	out, o	outlet
L	length (m)	p	pump
m	mass flow rate (kg/s)	preh	preheating
M_r	molecular weight (kg/kmol)	r	adverse flow; turning
n	exponent number	s	isentropic; shell; variable baffle spacing
N	number; lifetime	suph	superheating

P	pressure (Pa)	t	tube; expander; total
Pr	Prandtl number	tb	tube bundle
q	heat flux (W/m^2)	tcc	tube rows in crossflow
Q	heat capacity (W)	tcw	tube rows in baffle window
ΔP	pressure drop (Pa)	tp	tube pitch
Re	Reynolds number	vo	vapour only
r_f	fouling resistance	w	wall; window regions
R_p	surface roughness (m)	***Abbreviations***	
s	entropy (J/kg·K)	AD	absolute difference
T	temperature (K)	APR	area power ratio
v	fluid flow velocity (m/s)	CEPCI	chemical engineering plant cost index
W	power (W)	EPC	electricity production cost
X_{tt}	turbulent-turbulent Lockhart-Martinelli parameter	DPP	depreciated payback period
Z_t	number of tube passes	GWP	global warming potential
		HTC	heat transfer coefficient
Greek letters		HEPD	heat exchanger pressure drop
α	heat transfer coefficient (W/m^2·K)	HFOs	hydrofluoroolefins
ρ	density (kg/m^3)	ICE	internal combustion engine
μ	viscosity (Pa·s)	LMTD	logarithmic mean temperature difference
η	efficiency	ntm	tube numbers in the midline
φ	viscosity correction factor	NEDC	new European driving cycle
λ	thermal conductivity (W/m·K)	ODP	ozone depletion potential
δ	thickness (m)	ORC	organic Rankine cycle
γ	void fraction	RD	relative difference
Subscripts		SH	superheat degree
1-6	state point	SIC	specific investment cost
b	bundle bypass flow; baffle	WHR	waste heat recovery

1. Introduction

Stringent emission reduction and efficiency improvement regulations have imposed a significant pressure on the transportation sector and motivated original equipment manufacturers to consider a broad range of vehicle fuel-economy improvement solutions. As the main power generation component in vehicles, internal combustion engines (ICEs) convert chemical energy produced through fuel combustion into mechanical power. However, only 30-45% of the total chemical energy is used to produce effective power. The majority of the remaining energy is rejected as waste heat through the exhaust gases, the engine coolant circuit and the intake charge air cooler, which has been explicitly confirmed by Fu et al. [1] for a gasoline engine and Shu et al. [2] for a diesel engine, both based on energy balances on experimental test-data. Of these two heat sources, the exhaust gases, with their high temperature (and exergy), have the greatest potential to be recovered and converted into usable power mechanically or electrically, thereby reducing the fuel consumption and emissions of ICEs [3]. Waste-heat recovery (WHR) technologies for heat-to-power conversion have gained a growing interest in this regard [4,5], with organic Rankine cycles (ORCs) [6] appearing as a promising option for heat-source temperatures <400 °C and scales from as low as a few kWe to 10s of MWe in different applications [7,8].

Investigations on ORC technology for converting recovered waste-heat from ICEs have been conducted both computationally and experimentally [9,10], including on configuration design [11-13] and system optimization [14-16], working fluid selection by traditional pre-selection (including pure fluids [17,18] and mixtures [19,20]) and by new computer-aided molecular design methods [21-23] integrated into cycle optimization [24,25], expander selection and design [26,27] (including piston [28-30], screw [31-33] and rotary-vane [34] expanders), and off-design performance [35,36]. These excellent studies have enabled significant progress with the performance of ORC technology towards through careful considerations of the working fluid, key components and system parameters.

Heat exchangers, which are amongst of the key components of ORC systems since they play a significant role in both heat transfer processes, i.e., absorbing energy from heat source and rejecting heat to the heat sink, and directly influence the performance of ORC systems, have been studied by various investigators. Hatami et al. [37] presented a CFD modelling effort of an exhaust finned-tube heat exchanger for ICE-WHR, optimizing geometries to achieve maximum efficiency with a minimum pressure drop. Mastrullo et al. [38] proposed new concepts for compact heat exchangers in ORC systems by adopting a shell and louvered fin mini-tubes structure and more than 5% relative

pressure drop on the refrigerant side was observed for some specific geometries. Mokkapati and Lin [39] numerically studied corrugated-tube heat exchangers with twisted tapes for a heavy-duty diesel engine WHR system and results showed the heat transfer was enhanced by >230% compared to plain tube ones. Chen et al. [40] optimized a tube-in-tube exhaust heat-exchanger with metal-foam structures on the exhaust side to enhance gas-phase heat transfer, resulting heat transfer areas reduced to 1/3 of the original design with bare tube. However, Nematollahi et al. [41] reported that the pressure drop of the working fluid was 1.4-2.6 higher in a brazed metal-foam plate heat exchanger. Dynamic models have also been developed to capture the transient characteristics of ORC systems and heat exchangers during their operation under variable heat-source conditions [42]. Horst et al. [43] established moving boundary models for an exhaust heat exchanger while neglected pressure drops by stating that a small pressure drop (<10 mbar) was observed on their test bench. Similar work was reported by Feru et al. [44] for a plate-fin heat exchanger when studying two-phase heat transfer behaviour and by Shu et al. [45] for tube-in-tube heat exchangers when examining off-design ORC system (and heat exchanger) performance.

Beyond heat transfer enhancement, specific heat exchangers modelling and optimization efforts typically focus on heat exchanger sizing and costing for economic evaluations of ORC systems. Yu et al. [46] chose plate heat exchangers for a dual-loop ORC system and calculated the heat transfer areas. Galindo et al. [47] performed a multi-objective optimization of an ORC system using plate heat exchangers, although the pressure drop on the working fluid side was neglected. Yang et al. [48] selected a finned-tube evaporator for heat transfer with the exhaust gases and a plate-type condenser. Heat exchangers of fixed geometric dimensions were considered and the pressure drop was also ignored when conducting thermodynamic analyses. Yang and Yeh [49] selected shell-and-tube heat exchangers for an ORC system. Heat transfer areas were obtained by means of different heat transfer correlations, without mentioning pressure drops. Xia et al. [50] sized heat exchangers for a combined cooling and power system including an ORC, with a 2% pressure drop assumed in each heat exchanger. Similarly, Astolfi et al. [51] assumed that the pressure drop in the heat exchangers was either 2% of the inlet pressure or 50 kPa when comparing different ORC and CO_2 cycle systems. Chatzopoulou et al. [16] set a limit for the pressure drop through the heat exchanger of 10-60 kPa on the exhaust-gas side when sizing heat exchangers for an ORC system in an ICE WHR application. Tian et al. [52] conducted a thermo-economic analysis of ORC systems and set the heat exchanger pressure drop limit to 10 kPa, 20 kPa and 30 kPa for

the exhaust, the cooling water and the working fluid, respectively. Zhang et al. [53] also imposed assumed pressure drop allowances when sizing heat exchangers for ORC systems, with a 10 kPa limit in a plate type heat exchanger, a 20 kPa limit on the tube-side and a 30 kPa limit on the shell side of a shell-and-tube heat exchanger.

From the aforementioned studies, it can be seen that there is a knowledge gap between heat exchanger behaviour and ORC system performance, especially when it comes to an understanding of the interactions of the heat exchanger pressure drop with the overall ORC system and its thermo-economic performance indicators. The existing literature has either studied heat exchangers in isolation in order to enhance heat transfer performance and proposes various heat exchanger designs, or has focused exclusively on heat exchanger sizing and costing at given operating parameters, without accounting for pressure changes in the cycle analysis. However, heat exchangers are associated with both heat transfer and pressure drop, in general, and the effect of any effects of the heat exchanger pressure drop on the ORC system should be investigated rather than merely being ignored without evidence, especially in space-constrained applications where the number of components and their volume has to be reduced due to restrictions in costs, space and weight. Efforts to significantly enhance heat transfer typically result in larger pressure drops [54], while the operating cost of a heat exchanger is primarily reflected in the power to run fluid-moving devices such as pumps and fans [54]. When considering the pressure drop, more pumping power is required to drive the working fluid to the expected pressure, which results in an increased pumping power requirement since this is proportional to the heat exchanger pressure drop (HEPD). In addition, the pressure drop in the condenser will cause a backpressure in the expander, deteriorating the expander efficiency and reducing the generated power. Overall, in ORC systems, the pressure drop associated in the heat exchangers will inversely affect system performance from both thermodynamic and economic perspectives. Galindo et al. [55] presented results from a dynamic model of an ORC system with ethanol as the working fluid. Results showed that the ethanol side shows a 2-6 bar pressure drop while the exhaust pressure drop in the boiler shows a 5-20 mbar under the tested NEDC driving cycle, indicating that the HEPD should not be ignored in real applications.

Therefore, performance assessments and working-fluid selection exercises that do not explicitly consider the coupling between the HEPD and the performance of an associated ORC system may lead to sub-optimal results and can overestimate the capabilities of such systems

relative to practical experience. In order to close this gap between the HEPD and the results of ORC assessments, this paper proposes an improved approach for thermo-economic analyses of ORC systems that will be particularly relevant in space-constrained applications. After comparing the new approach and conventional methods where the HEPD is ignored, the thermo-economic performance of ORC systems employing heat exchangers with various cross-sections is fully examined. Different working fluids with low global warming potential (GWP), e.g., HFOs, are also considered. These results reveal design conflicts that arise from opposing thermal performance, pressure drop and economic performance requirements in ORC systems, and that the proposed approach enhances the reliability and accuracy of system design and analysis.

2. Modelling methodology

A typical subcritical non-recuperative ORC system is adopted to study the interaction of the heat exchanger pressure drop (HEPD) with the ORC system performance; Fig. 1 shows a schematic ORC system layout and corresponding *T*-*s* diagram. The working fluid is first pressurized in a pump (Process 1-2). Then it is heated to a saturated vapour in an evaporator through the preheating Process 2-3 and then evaporated through a flow boiling Process 3-4. After expansion in an expander (4-5), the working fluid enters a condenser where it is first de-superheated (5-6) and then condensed (6-1) by transferring heat to a flow of cooling water.

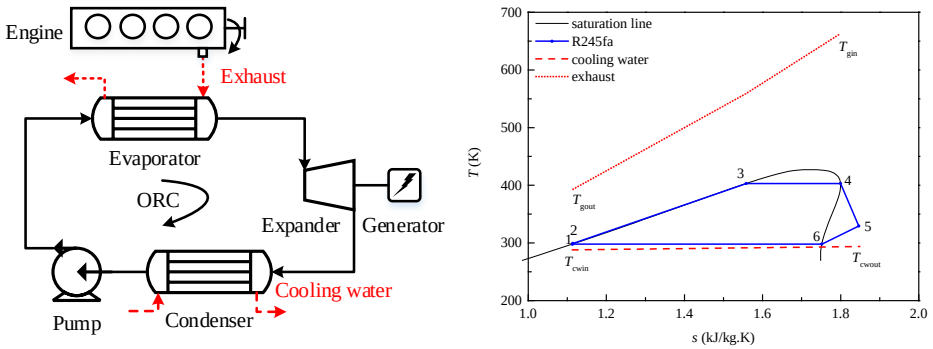

(a) Schematic diagram. (b) Thermodynamic cycle (*T*-*s*) diagram.

Figure 1. Definition of the subcritical, non-recuperative ORC system considered in the present study.

The heat source for the ORC system is the exhaust-gas stream of a typical inline, 4-stroke, 6-cylinder 5.1-L diesel engine (YCK05230) made by the Guangxi Yuchai Machinery Group. The

ICE's rated power is 169 kW and its rated speed is 2200 rpm. Heat balance tests were conducted to obtain the exhaust characteristics under conditions that cover the whole engine map. Although the ICE's load point changes over the drive cycle, resulting in an exhaust temperature, mass flow rate and composition that vary as a function of the engine speed and torque, it is assumed in our work that for the majority of the time the ICE operates at a specific engine load, which corresponds to ORC system design point. Specifically, we take this nominal design point to correspond to averaged values obtained from the lowest brake specific fuel consumption (BSFC) condition zones of the ICE considered in the current study. The mass flow rate and temperature of the exhaust gases are set to constant values of 0.13 kg/s and 663 K, respectively. The exhaust gas mainly consists of four compositions: N_2, O_2, CO_2 and H_2O, with the mass fractions of 73.0%, 5.8%, 15.2% and 6.0%, respectively. The minimum temperature of the exhaust gas in the evaporator is set to be 393 K to avoid any corrosion in the evaporator.

2.1. ORC thermodynamic model

An ORC model was developed in MATLAB, with fluid properties obtained from REFPROP 9.1. In this model, the isentropic efficiency of the pump is set to a fixed value of 0.8 [13,18] while that of the expander is set to a fixed value 0.7 [12,14]. The pinch point temperature difference in the evaporator is 30 K while that in the condenser is 5 K. The condensation temperature, ambient temperature and ambient pressure are fixed at 298 K, 288 K and 101.3 kPa, respectively. The parametric calculation of the thermodynamic performance of the ORC system can be briefly summarized with the following equations [21-23].

$$W_{\mathrm{p}} = m_{\mathrm{f}} \cdot \left(h_2 - h_1\right) = m_{\mathrm{f}} \cdot \left(h_{2\mathrm{s}} - h_1\right) / \eta_{\mathrm{p}} \tag{1}$$

$$Q_{\mathrm{e}} = m_{\mathrm{f}} \cdot \left(h_3 - h_2\right) = m_{\mathrm{g}} \cdot c_{\mathrm{p,g}} \cdot \left(T_{\mathrm{g,in}} - T_{\mathrm{g,out}}\right) \tag{2}$$

$$W_{\mathrm{e}} = m_{\mathrm{f}} \cdot \left(h_4 - h_5\right) = m_{\mathrm{f}} \cdot \left(h_4 - h_{5\mathrm{s}}\right) \cdot \eta_{\mathrm{e}} \tag{3}$$

$$Q_{\mathrm{c}} = m_{\mathrm{f}} \cdot \left(h_5 - h_1\right) = m_{\mathrm{cw}} \cdot c_{\mathrm{p,cw}} \cdot \left(T_{\mathrm{cw,out}} - T_{\mathrm{cw,in}}\right) \tag{4}$$

$$W_{\mathrm{net}} = W_{\mathrm{e}} - W_{\mathrm{p}} \tag{5}$$

where m denotes a mass flow rate; h a specific enthalpy; T and P are temperatures and pressures, respectively; Q_{e} and Q_{c} are the heat duty of the evaporator and the condenser, respectively; W_{p}, W_{e} and W_{net} are the pump power consumption, the expansion power output and the net power output

from the system, respectively; η_p and η_e are the (fixed [15,17]) isentropic efficiencies of the pump and the expander; c_p is a specific heat capacity. Furthermore, subscripts '1'-'6' denote thermodynamic states; 'f', 'g' and 'cw' refer to the working fluid, exhaust gas and cooling water, respectively; 'in' and 'out' to the inlet and outlet; and 's' signifies an isentropic process.

Conventionally, the pressure drop is neglected in components and pipes when conducting state parameters computation based on the first law of thermodynamics. Therefore, pressures at the main state points are expressed as:

$$P_2 = P_3 = P_4 = P_{evap} \tag{6}$$

$$P_5 = P_6 = P_1 = P_{cond} \tag{7}$$

The thermophysical properties of the working fluid (e.g,. temperature, density, enthalpy and entropy) are then calculated. After obtaining all the state parameters, thermo-economic analysis can be further carried on through sizing heat exchangers and costing each component. Figure 2(a) illustrates a conventional approach for the thermo-economic analysis of an ORC system. The sizing of heat exchangers can be achieved by discretizing the heat exchanger into several sub-sections and calculating the corresponding heat transfer coefficient by applying the relevant heat transfer correlations. Generally, mass flow rate, inlet temperature and pressure of the working fluid and the secondary fluid, and heat capacity are required for calculating the required heat transfer area. The logarithmic mean temperature difference (LMTD) method is applied during this process. However, the estimated pressure drop of heat exchangers is set aside.

This work proposes an improved procedure for the thermo-economic analysis of ORC systems, as demonstrated in Fig. 2(b), which is expected to be more relevant in space-constrained applications. The difference lies in the handling of the HEPD compared to conventional methods. In our approach, the evaluated pressure drop is fed back to the cycle calculation, modifying the cycle in an iterative procedure. The procedure terminated only when the pressures in the cycle match the pressure drop caused by the heat exchanger design models. In this way, the heat exchanger behaviour and the cycle are effectively coupled with each other, which leads to results that are expected to be more practically relevant and reliable. To simplify the modelling of the pressure variation at each location along the heat exchangers tubes or plates, the pressure drop is taken into consideration by raising the inlet pressures of the heat exchangers. The outlet pressure of the evaporator is assumed to be the evaporation pressure (P_{evap}). The outlet pressure of the condenser is assumed to be the condensation pressure (P_{cond}). The pressures at each state are listed

in Eqs. (8)-(13), substituting Eq. (6) and Eq. (7), and further used to calculate other thermophysical properties of the working fluid:

$$P_1 = P_{\text{cond}} \tag{8}$$

$$P_2 = P_3 + \Delta P_{\text{f,preh}} \tag{9}$$

$$P_3 = P_4 + \Delta P_{\text{f,evap}} \tag{10}$$

$$P_4 = P_{\text{evap}} \tag{11}$$

$$P_5 = P_6 + \Delta P_{\text{f,desup}} \tag{12}$$

$$P_6 = P_1 + \Delta P_{\text{f,cond}} \tag{13}$$

wherein ΔP refers to the pressure drop through each section; subscripts 'preh', 'evap', 'desup' and 'cond' refer to the preheating section and evaporation section in the evaporator, de-superheating section and condensation section in the condenser, respectively.

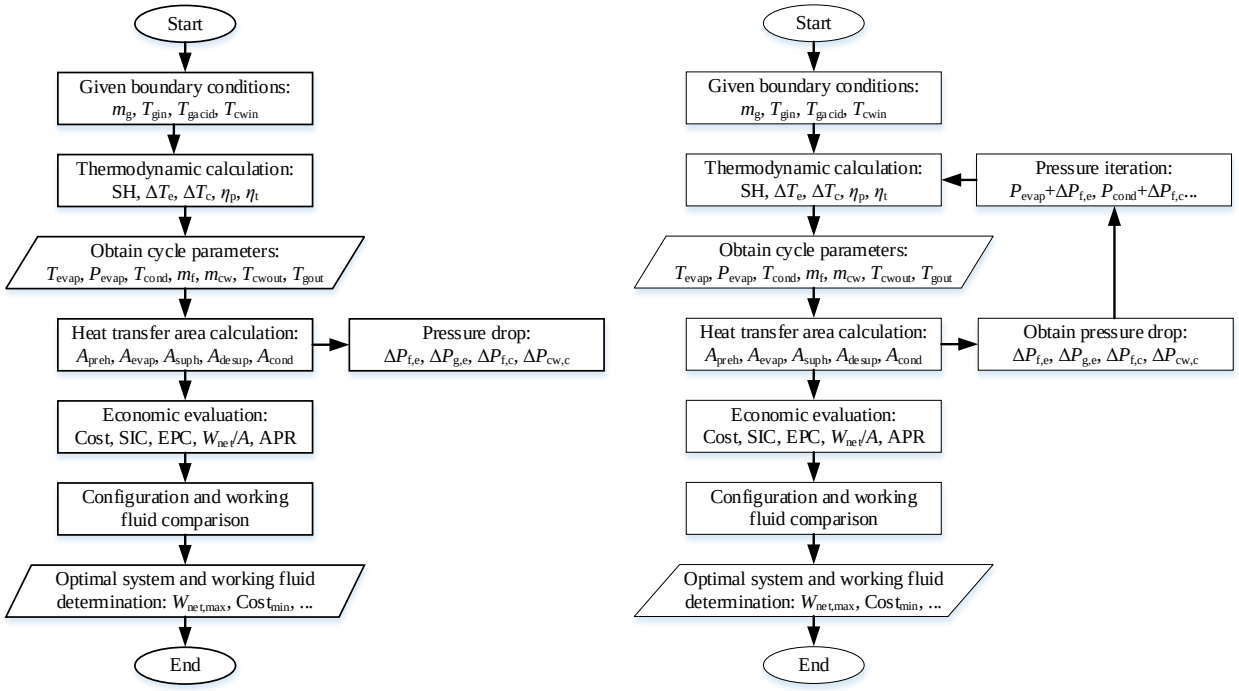

(a) Conventional approach (without HEPD). (b) Improved approach (with HEPD).

Figure 2. Alternative procedures for the thermo-economic analysis of ORC systems.

2.2. Heat exchanger sizing

The most commonly employed heat exchanger type is the shell-and-tube heat exchanger, which is chosen here for both heat transfer components in our investigated ORC system. TEMA standards are followed for the design of the shell-and-tube heat exchangers.

The total heat transfer area is calculated from the following equations [54]:

$$A = \frac{Q}{K \cdot \mathrm{LMTD}} \tag{14}$$

$$\frac{1}{K} = \frac{1}{\alpha_\mathrm{t}} \cdot \frac{d_\mathrm{o}}{d_\mathrm{i}} + r_\mathrm{ft} \cdot \frac{d_\mathrm{o}}{d_\mathrm{i}} + \frac{\delta_\mathrm{w}}{\lambda_\mathrm{w}} \cdot \frac{d_\mathrm{o}}{d_\mathrm{m}} + r_\mathrm{fs} + \frac{1}{\alpha_\mathrm{s}} \tag{15}$$

$$\mathrm{LMTD} = \frac{\left(T_\mathrm{h,in} - T_\mathrm{c,out}\right) - \left(T_\mathrm{h,out} - T_\mathrm{c,in}\right)}{\ln\left[\left(T_\mathrm{h,in} - T_\mathrm{c,out}\right) / \left(T_\mathrm{h,out} - T_\mathrm{c,in}\right)\right]} \tag{16}$$

where Q is the heat capacity; K is the overall heat transfer coefficient; LMTD is the logarithmic mean temperature difference for the flows; α_t and α_s are the heat transfer coefficients on the tube side and the shell side; λ_w and δ_w are the wall resistance and the wall thickness; d_o, d_i, d_m are outside diameter, inside diameter and mean diameter of the tubes; r_ft and r_fs are the fouling resistances on the tube side and the shell side; T is temperature. Subscripts ‘h’ and ‘c’ denote the hot fluid side and the cold fluid side, and ‘in’ and ‘out’ refer to the inlet and outlet.

2.2.1. Shell side

Bell-Delaware method [54] is applied here to calculate various geometric parameters for the determination of shell side heat transfer coefficient and pressure drop. An ideal crossflow heat transfer coefficient (α_si) is firstly calculated using Eq. (17) and Eq. (18), and then modified for the presence of each stream through correction factors:

$$\alpha_\mathrm{si} = j_\mathrm{i} \cdot \frac{c_\mathrm{p,s} \cdot G_\mathrm{s}}{\mathrm{Pr}_\mathrm{s}^{2/3}} \cdot \left(\frac{\mu_\mathrm{s}}{\mu_\mathrm{w}}\right)^{0.14} \tag{17}$$

$$j_\mathrm{i} = \begin{cases} 1.73 \cdot \mathrm{Re}_\mathrm{s}^{-0.694} & \left(1 \le \mathrm{Re}_\mathrm{s} < 100\right) \\ 0.717 \cdot \mathrm{Re}_\mathrm{s}^{-0.574} & \left(100 \le \mathrm{Re}_\mathrm{s} < 1000\right) \\ 0.236 \cdot \mathrm{Re}_\mathrm{s}^{-0.346} & \left(\mathrm{Re}_\mathrm{s} \ge 1000\right) \end{cases} \tag{18}$$

where Re is Reynolds number; Pr is Prandtl number; G is mass flow flux; c_p means specific heat capacity; μ_s and μ_w are viscosity at bulk mean temperature and wall temperature, respectively.

Therefore, the shell side heat transfer coefficient is given by:

$$\alpha_s = \alpha_{si} \cdot j_c \cdot j_l \cdot j_b \cdot j_s \cdot j_r \tag{19}$$

where j_c, j_l, j_b, j_s, j_r are the correction factor for baffle cut and spacing, for baffle leakage effects, for bundle bypass flow, for variable baffle spacing in the inlet and outlet sections, and for adverse temperature gradient build-up in laminar flow, respectively. The calculation of these correction factors can be found in Ref. [54].

The total shell side pressure drop (ΔP_s) consists of the pressure drop due to crossflow (ΔP_c), window regions (ΔP_w), and entrance and exit sections (ΔP_e), and is calculated from [54]:

$$\Delta P_s = \Delta P_c + \Delta P_w + \Delta P_e \tag{20}$$

$$\Delta P_c = (N_b - 1) \cdot \Delta P_{bi} \cdot R_b \cdot R_l \tag{21}$$

$$\Delta P_w = \Delta P_{wi} \cdot N_b \cdot R_l \tag{22}$$

$$\Delta P_e = 2 \cdot \Delta P_{bi} \cdot \left(1 + \frac{N_{tcw}}{N_{tcc}}\right) R_b \cdot R_s \tag{23}$$

$$\Delta P_{bi} = \frac{2 \cdot f_s \cdot N_{tcc} \cdot G_s^2}{\rho_s} \cdot \left(\frac{\mu_s}{\mu_w}\right)^{-0.14} \tag{24}$$

$$\Delta P_{wi} = \begin{cases} \dfrac{(2 + 0.6 \cdot N_{tcw}) \cdot G_w^2}{2 \cdot \rho_s} & (\mathrm{Re}_s \geq 100) \\ \dfrac{26 \cdot G_w \cdot \mu_s}{\rho_s} \left(\dfrac{N_{tcw}}{L_{tp} - d_o} + \dfrac{L_{bc}}{D_w^2}\right) + \dfrac{2 \cdot G_w^2}{\rho_s} & (\mathrm{Re}_s < 100) \end{cases} \tag{25}$$

$$f_s = \begin{cases} \dfrac{52}{\mathrm{Re}_s} + 0.17 & (1 \leq \mathrm{Re}_s < 500) \\ 0.56 \cdot \mathrm{Re}_s^{-0.14} & (\mathrm{Re}_s \geq 500) \end{cases} \tag{26}$$

where f_s is the friction factor; ρ is the density; L_{tp} is tube pitch; L_{bc} is central baffle spacing; G_w is the window mass flux; D_w is the equivalent hydraulic diameter of a segmental baffle window; N_b, N_{tcc} and N_{tcw} are the number of baffles, the number of effective tube rows in crossflow, and the number of effective tube rows in baffle window; R_b, R_l and R_s are correction factors for bundle bypass effects, for baffle leakage effects and for unequal baffle spacing at inlet and outlet, respectively. Detailed calculation for these factors can be found in Ref. [54].

2.2.2. Tube side

Empirical heat transfer correlations are used to estimate the tube-side heat transfer coefficient. The Dittus-Boelter correlation is used for the single-phase zone (preheating and de-superheating) [54]:

$$\alpha_{\mathrm{t}} = 0.023 \cdot \frac{\lambda}{d_{\mathrm{i}}} \mathrm{Re}^{0.8} \cdot \mathrm{Pr}^{n} \tag{27}$$

where λ is thermal conductivity; and also where $n = 0.4$ for heating and $n = 0.3$ for cooling.

The Cooper nucleate pool-boiling method is used for the evaporation zone [17]:

$$\alpha_{\mathrm{t}} = 1.5 \cdot 55 \cdot \left(P_{\mathrm{evap}} / P_{\mathrm{crit}} \right)^{\left[0.12 - 0.2 \cdot \log\left(R_{\mathrm{p}} \right) \right]} \cdot \left[-\log(P_{\mathrm{evap}} / P_{\mathrm{crit}}) \right]^{-0.55} \cdot q^{0.67} \cdot M_{\mathrm{r}}^{-0.5} \tag{28}$$

where P_{crit} is the critical pressure of the working fluid; R_{p} is the surface roughness; q is the heat flux; and M_{r} is the molecular weight of the working fluid.

The Dobson correlation [56] is used for the condensation process. For mass fluxes $G \geq 500\ \mathrm{kg/m^2 \cdot s}$ we use Eq. (29), whereas for $G < 500\ \mathrm{kg/m^2 \cdot s}$ we use Eq. (29) if $\mathrm{Fr_{so}} > 20$:

$$\alpha_{\mathrm{t}} = 0.023 \cdot \frac{\lambda}{d_{\mathrm{i}}} \cdot \mathrm{Re}_{\mathrm{l}}^{0.8} \cdot \mathrm{Pr}_{\mathrm{l}}^{0.4} \cdot \left(1 + \frac{2.22}{\mathrm{X}_{\mathrm{tt}}^{0.89}} \right) \tag{29}$$

and Eq. (30) if $\mathrm{Fr_{so}} < 20$:

$$\alpha_{\mathrm{t}} = \frac{\lambda}{d_{\mathrm{i}}} \cdot \left[\frac{0.23 \cdot \mathrm{Re}_{\mathrm{vo}}^{0.12}}{1 + 1.11 \cdot \mathrm{X}_{\mathrm{tt}}^{0.58}} \left(\frac{\mathrm{Ga} \cdot \mathrm{Pr}_{\mathrm{l}}}{\mathrm{Ja}_{\mathrm{l}}} \right)^{0.25} + \frac{\arccos\left(2 \cdot \gamma - 1 \right)}{\pi} \cdot \mathrm{Nu}_{\mathrm{forced}} \right] \tag{30}$$

where $\mathrm{Fr_{so}}$ is Soliman's-modified Froude number; $\mathrm{X_{tt}}$ is turbulent-turbulent Lockhart-Martinelli parameter; $\mathrm{Re_l}$ is the superficial liquid Reynolds number; $\mathrm{Pr_l}$ is liquid Prandtl number; $\mathrm{Re_{vo}}$ is vapour-phase Reynolds number; Ga is Galileo number; $\mathrm{Ja_l}$ is liquid Jakob number; γ is void fraction; and $\mathrm{Nu_{forced}}$ is the forced-convective Nusselt number. These can be calculated from [56]:

$$\mathrm{Fr_{so}} = \begin{cases} 0.025 \cdot \mathrm{Re}_{\mathrm{l}}^{1.59} \cdot \left(\dfrac{1 + 1.09 \cdot \mathrm{X}_{\mathrm{tt}}^{0.039}}{\mathrm{X}_{\mathrm{tt}}} \right)^{1.5} \cdot \dfrac{1}{\mathrm{Ga}^{0.5}} & \left(\mathrm{Re_l} \leq 1250 \right) \\ 1.26 \cdot \mathrm{Re}_{\mathrm{l}}^{1.04} \cdot \left(\dfrac{1 + 1.09 \cdot \mathrm{X}_{\mathrm{tt}}^{0.039}}{\mathrm{X}_{\mathrm{tt}}} \right)^{1.5} \cdot \dfrac{1}{\mathrm{Ga}^{0.5}} & \left(\mathrm{Re_l} > 1250 \right) \end{cases} \tag{31}$$

$$\mathrm{X}_{\mathrm{tt}} = \left(\frac{\rho_{\mathrm{g}}}{\rho_{\mathrm{l}}} \right)^{0.5} \cdot \left(\frac{\mu_{\mathrm{l}}}{\mu_{\mathrm{g}}} \right)^{0.1} \cdot \left(\frac{1 - x}{x} \right)^{0.9} \tag{32}$$

$$\mathrm{Re}_{\mathrm{l}} = \frac{G \cdot d_{\mathrm{i}} \cdot \left(1 - x \right)}{\mu_{\mathrm{l}}} \tag{33}$$

$$\mathrm{Pr_l} = \frac{\mu_\mathrm{l} \cdot c_\mathrm{p,l}}{\lambda_\mathrm{l}} \tag{34}$$

$$\mathrm{Re_{vo}} = \frac{G \cdot d_\mathrm{i}}{\mu_\mathrm{g}} \tag{35}$$

$$\mathrm{Ga} = \frac{g \cdot \rho_\mathrm{l} \cdot \left(\rho_\mathrm{l} - \rho_\mathrm{g}\right) d_\mathrm{i}^3}{\mu_\mathrm{l}^2} \tag{36}$$

$$\mathrm{Ja_l} = \frac{c_\mathrm{p,l} \cdot \left(T_\mathrm{sat} - T_\mathrm{w}\right)}{h_\mathrm{lg}} \tag{37}$$

$$\mathrm{Nu_{forced}} = 0.0195 \cdot \mathrm{Re_l^{0.8}} \cdot \mathrm{Pr_l^{0.4}} \cdot \sqrt{1.376 + \frac{c_1}{\mathrm{X_{tt}^{c_2}}}} \tag{38}$$

$$\mathrm{Fr_l} = \frac{G^2}{\rho_\mathrm{l}^2 \cdot g \cdot d_\mathrm{i}} \tag{39}$$

$$c_1 = \begin{cases} 4.172 + 5.48 \cdot \mathrm{Fr_l} - 1.564 \cdot \mathrm{Fr_l^2} & \left(0 < \mathrm{Fr_l} \le 0.7\right) \\ 7.242 & \left(\mathrm{Fr_l} > 0.7\right) \end{cases} \tag{40}$$

$$c_2 = \begin{cases} 1.773 - 0.169 \cdot \mathrm{Fr_l} & \left(0 < \mathrm{Fr_l} \le 0.7\right) \\ 1.655 & \left(\mathrm{Fr_l} > 0.7\right) \end{cases} \tag{41}$$

Finally, for the pressure drop on the tube side, the total pressure drop (ΔP_t) consists of the pressure drop through the tube bundle (ΔP_tb), the pressure drop in the nozzles (ΔP_n), sudden contraction and expansion losses at the entry and exit ($\Delta P_\mathrm{c,e}$), and the pressure drop associated with the turning losses (ΔP_r). They are expressed as follows [54]:

$$\Delta P_\mathrm{t} = \Delta P_\mathrm{tb} + \Delta P_\mathrm{n} + \Delta P_\mathrm{c,e} + \Delta P_\mathrm{r} \tag{42}$$

$$\Delta P_\mathrm{tb} = \frac{f_\mathrm{t} \cdot L \cdot G^2 \cdot Z_\mathrm{t}}{2 \cdot d_\mathrm{i} \cdot \rho \cdot \varphi_\mathrm{t}} \tag{43}$$

$$\Delta P_\mathrm{n} = \frac{1.5 \cdot G^2}{2 \cdot \rho} \tag{44}$$

$$\Delta P_\mathrm{c,e} = \frac{G^2}{2 \cdot \rho} \cdot \left(K_\mathrm{c} + K_\mathrm{e}\right) \cdot Z_\mathrm{t} \tag{45}$$

$$\Delta P_\mathrm{r} = \frac{4 \cdot Z_\mathrm{t} \cdot G^2}{2 \cdot \rho} \tag{46}$$

where f_t is the friction factor; L is the tube length; Z_t is the number of passes; K_c and K_e are the contraction and expansion loss coefficients; and φ_t is a parameter related to the ratio of the viscosity

evaluated at the bulk mean temperature and at the wall temperature.

2.3. ORC economic model

In this paper, the net power output per unit heat exchanger area (W_{net}/A) is used as an important economic indicator to explicitly address the influence of the HEDP on system performance. Furthermore, we also estimate the specific investment cost (SIC) and depreciated payback period (DPP) of the ORC systems. Since there are different costing models with varying levels of accuracy and a lack of commercial data for small-scale power plants similar to the ORC systems of around 5 kWe considered in this paper, a preliminary estimation of the systems' capital costs is obtained by adopting the module costing method typically used for chemical power plants [57], and which has been extensively used in the literature for ORC system cost estimations [46,49,50]. Table 1 lists the relevant cost models used for each component, where the equipment capacity is applied into simple relationships. The pump is taken to be a centrifugal type and the expander is an axial type turbine.

Table 1. Models for ORC system cost estimation [57].

	Bare module cost models	Coefficients
Heat exchanger	$\log\left(C_{\mathrm{p}}^{0}\right)=K_1+K_2\cdot\log\left(A\right)+K_3\cdot\left[\log\left(A\right)\right]^2$ $\log\left(F_{\mathrm{p}}\right)=C_1+C_2\cdot\log\left(P\right)+C_3\cdot\left[\log\left(P\right)\right]^2$ $C_{\mathrm{BM}}=C_{\mathrm{p}}^{0}\cdot\left(B_1+B_2\cdot F_{\mathrm{M}}\cdot F_{\mathrm{p}}\right)$	K_1 = 4.3247; C_1 = -0.0016; K_2 = -0.3030; C_2 = -0.0063; K_3 = 0.1634; C_3 = 0.0123; B_1 = 1.63; B_2 = 1.66; F_{M} = 1.35;
Pump	$\log\left(C_{\mathrm{p}}^{0}\right)=K_1+K_2\cdot\log\left(W_{\mathrm{p}}\right)+K_3\cdot\left[\log\left(W_{\mathrm{p}}\right)\right]^2$ $\log\left(F_{\mathrm{p}}\right)=C_1+C_2\cdot\log\left(P\right)+C_3\cdot\left[\log\left(P\right)\right]^2$ $C_{\mathrm{BM}}=C_{\mathrm{p}}^{0}\cdot\left(B_1+B_2\cdot F_{\mathrm{M}}\cdot F_{\mathrm{p}}\right)$	K_1 = 3.3892; C_1 = -0.3935; K_2 = 0.0536; C_2 = 0.3957; K_3 = 0.1538; C_3 = -0.0023; B_1 = 1.89; B_2 = 1.35; F_{M} = 1;
Expander	$\log\left(C_{\mathrm{p}}^{0}\right)=K_1+K_2\cdot\log\left(W_{\mathrm{e}}\right)+K_3\cdot\left[\log\left(W_{\mathrm{e}}\right)\right]^2$ $C_{\mathrm{BM}}=C_{\mathrm{p}}^{0}\cdot F_{\mathrm{BM}}$	K_1 = 2.7051; K_2 = 1.4398; K_3 = -0.1776; F_{BM} = 3.5;

Based on the component costs, the specific investment cost (SIC), the electricity production cost (EPC) [46] and the depreciated payback period (DPP) [53] of the system can be obtained:

$$C_{\text{in}} = \sum C_{\text{BM}} \cdot \frac{\text{CEPCI}_{2017}}{\text{CEPCI}_{2001}} \tag{47}$$

$$\text{SIC} = C_{\text{in}} / W_{\text{net}} \tag{48}$$

$$\text{EPC} = \frac{C_{\text{ann}} + \dfrac{i \cdot (1+i)^N}{(1+i)^N - 1} C_{\text{in}}}{W_{\text{net}} \cdot hr_{\text{full\_load}}} \tag{49}$$

$$\text{DPP} = \ln\left(\frac{W_{\text{net}} \cdot hr_{\text{full\_load}} \cdot C_{\text{elec}} - C_{\text{ann}}}{W_{\text{net}} \cdot hr_{\text{full\_load}} \cdot C_{\text{elec}} - C_{\text{ann}} - k \cdot C_{\text{in}}} \right) / \ln(1+k) \tag{50}$$

where C_{in} is the initial investment cost of the system; C_{ann} the annual operation and maintenance cost, set as 1.65% of the investment cost [46]; C_{elec} the electricity price, set as 0.3 $/kWh; N the lifetime of the system; i the interest rate, set as 5% [46]; k the discount rate, set as 5% [46]; $hr_{\text{full\_load}}$ the full-load operation hours, set as 7500 h [46]; CEPCI the chemical engineering plant cost index; here CEPCI_{2001} = 397.0 and CEPCI_{2017} = 567.5 [58].

2.4. Model validation

The ORC model based on conventional approaches was validated against Ref. [53]. The boundary conditions (heat source/sink temperatures, pressure drop limits, etc.) and other parameters (pump/expander isentropic efficiencies, pinch point temperatures, condensing temperature, etc.) were set to the same values as in Ref. [53]. Two different cases were considered for both R600 and R601. Case 1 refers to the scenario where the minimum heat source temperature should be >82 °C. Case 2 refers to the scenario where there is no limitation for the heat source temperature. The comparative results of EPC and DPP are given in Fig. 3. It can be seen clearly that the simulation results from the present models are in good agreement with the reference, which gives confidence in the validity of these models and the engineering-level prediction results reported in this work.

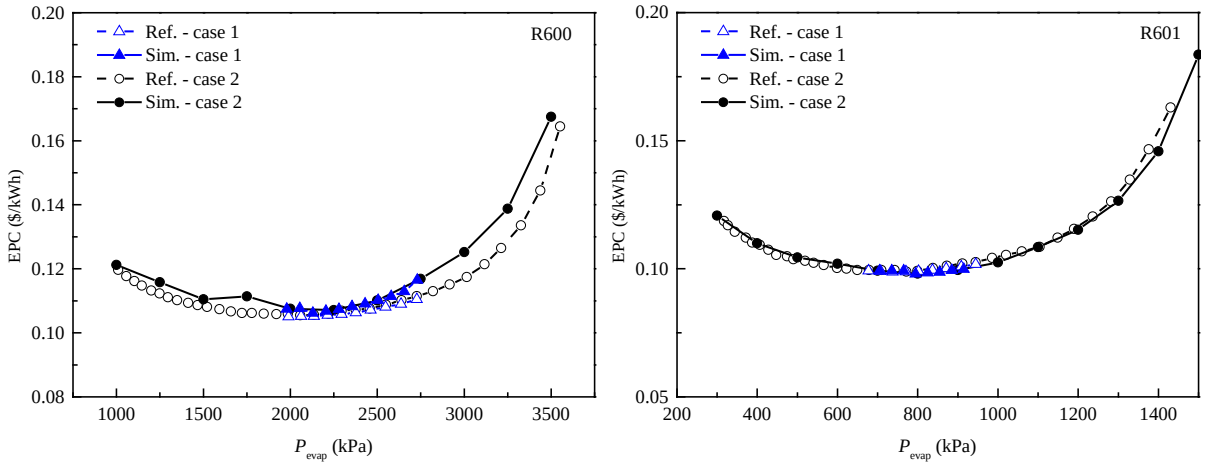

(a) Results of electricity production cost (EPC).

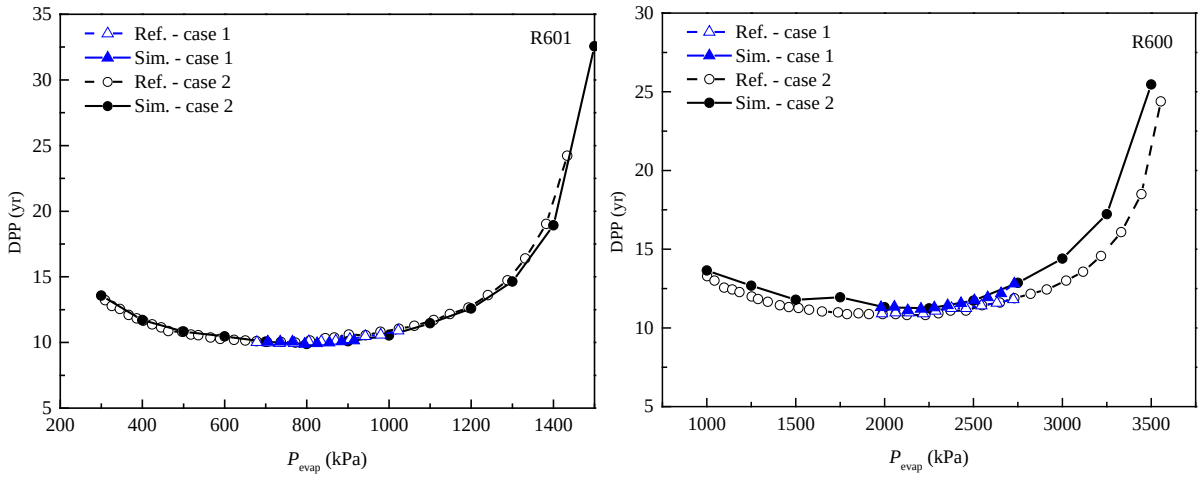

(b) Results of depreciated payback period (DPP).

Figure 3. Model validation against data from Ref. [53].

3. Results and discussion

3.1. ORC system performance

In this section, we compare results from adopting our proposed approach for ORC system modelling to those generated by using conventional methods. The net power output (W_{net}) is used to indicate the ORC system's thermodynamic performance, while the net power output per unit heat exchanger area (W_{net}/A) is used as an economic indicator. R245fa is considered here as the working fluid as it is a well-known fluid that has been extensively investigated in the literature and that is currently being used in many ORC systems for its good performance [16].

Figure 4(a) shows the variations of the pumping power (W_p), expansion power (W_e) and net power output (W_{net}) from the investigated ORC system with R245fa as the working fluid, at different evaporation temperatures (and pressures). It can be observed that the HEPD causes a reduction in W_e, and raises the pump power consumption slightly. If we take the evaporation temperature of 403 K as an example, W_e decreases from 5.28 kW to 4.81 kW, showing an overestimation of 0.47 kW (corresponding to 10% in the predicted power) if the HEPD is ignored. There is only a slight change in W_p, which increases from 307.2 W to 307.3 W.

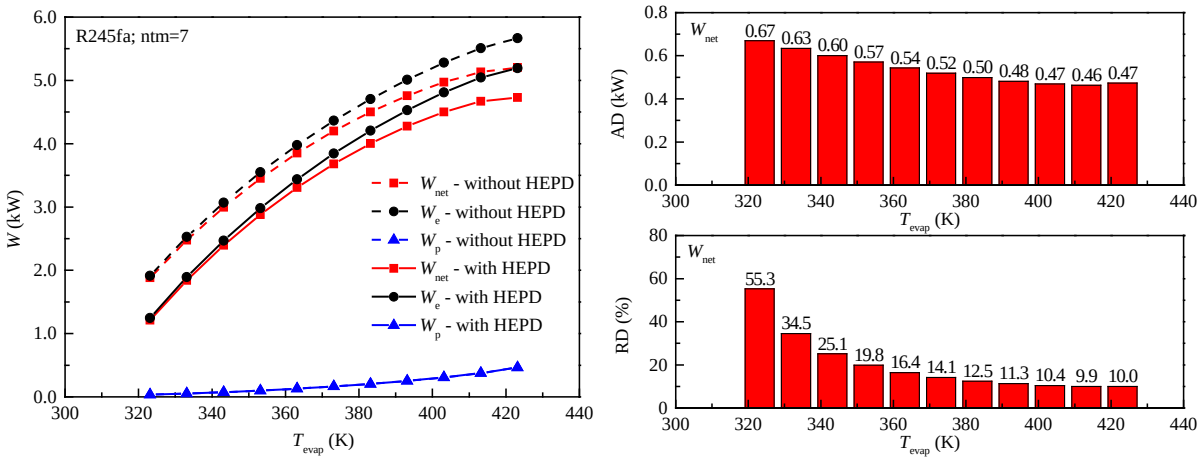

(a) Variations of system power with T_{evap}. (b) Absolute and relative differences in W_{net}.

Figure 4. Difference in ORC system power predictions between the two approaches illustrated in Fig. 2 (with and without HEPD) over a range of different evaporation temperatures T_{evap}.

This can be explained based on the following considerations: (1) The evaporator consists of a preheating zone and an evaporating zone, where the exhaust transfers heat to liquid-phase and two-phase working fluid, respectively. R245fa shows lower velocities in the tubes due to higher density, thus resulting in a lower pressure drop since the pressure drop is proportional to the square of the fluid velocity. (2) In the condenser, especially in the de-superheater, the average density of R245fa in the de-superheating process (8.1 kg/m^3) is much smaller than that in the preheating process (1140 kg/m^3), which leads to a dramatic rise in the velocity and a higher pressure drop in the de-superheater. (3) According to Eq. (14), the smaller LMTD results in larger heat transfer area requirements for the condenser, which is reflected in the length of the tubes. This leads to a larger pressure drop in the condenser than in the evaporator since the pressure drop through the tube bundle is proportional to its length. (4) The pressure drop in the evaporator requires more pumping

power while the pressure drop in the condenser causes higher backpressure in the expander and reduces power generation. Table 2 gives the main parameters of the heat exchangers related to these explanations.

Table 2. Main heat exchangers parameters when ignoring the HEPD.

	Preheating	Evaporation	De-superheating	Condensation
T_{in} (K)	299	403	329	298
P_{in} (kPa)	2340	2340	148	148
ρ_{in} (kg/m^3)	1340	940	7.6	8.6
T_{out} (K)	403	403	298	298
P_{out} (kPa)	2340	2340	148	148
ρ_{out} (kg/m^3)	940	155	8.6	1340
Q (kW)	23.4	14.6	4.5	28.6
K (kW/m^2·K)	0.19	0.41	0.35	1.25
LMTD (K)	123	204	16	7
v (m/s)	0.14	0.61	20.1	9.49
ΔP (kPa)	0.2	0.6	28.6	13.6

In addition, Fig. 4 also indicates that the predicted differences in the net power output become smaller as the evaporation temperature (T_{evap}) increases, as does the power generated by the expander. The absolute differences (ADs) in W_{net} decrease from 0.67 kW to 0.47 kW and the corresponding relative differences (RDs), i.e., relative to the calculations which account for the HEPD, decrease from 55.3% to 10.0% as T_{evap} increases from 323 K to 423 K. This suggests that the HEPD should be considered especially at low evaporation temperatures. Since the condensation temperature is fixed at 298 K, the performance of the ORC system is mainly related to T_{evap}; the higher T_{evap}, the lower the mass flow rate of the working fluid in the ORC system, which results in a smaller pressure drop in both the evaporator and condenser (due to $\Delta P \propto G^2$). Moreover, sensible heat transfer accounts for a larger fraction of the overall heat addition process at higher T_{evap}, which causes smaller pressure drops in the evaporator due to higher densities and, thus, lower flow speeds of the working fluid in the liquid phase. In the condenser, although the inlet temperature to this component increases at higher T_{evap}, the decrease in the mass flow rate

dominates, therefore leading to a smaller pressure drop of the working fluid through the condenser, as shown in Fig. 5.

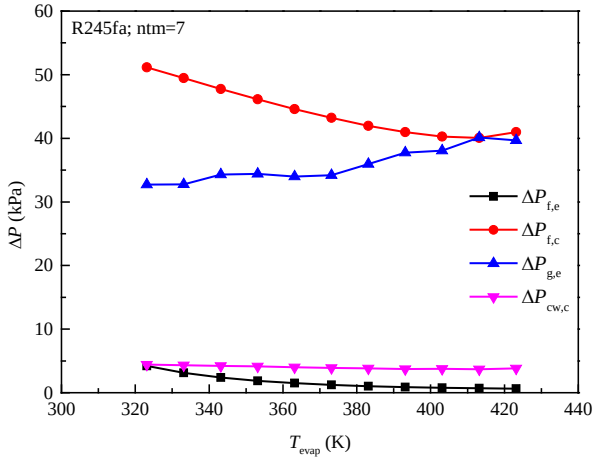

Figure 5. Heat exchanger pressure drops in the ORC system at different evaporation temperatures.

Figure 6(a) shows the net power output per unit heat transfer area (W_{net}/A), which is selected as an index for the economic performance of ORC systems, as a function of the evaporation temperature; the corresponding absolute differences (ADs) and relative differences (RDs) are shown in Fig. 6(b). Similar with the variation of W_{net}, we observed that W_{net}/A is lower if HEPDs are considered in the cycle calculation and that the differences decrease at higher T_{evap}. If we take the evaporation temperature of 403 K as an example, W_{net}/A decreases from 0.97 kW/m^2 to 0.83 kW/m^2, showing an overestimation of 0.14 kW/m^2 (corresponding to 16% in the predicted W_{net}/A) if the HEPD is ignored. While at a lower evaporation temperature of 323 K, W_{net}/A decreases from 0.40 kW/m^2 to 0.24 kW/m^2, showing an overestimation of 0.16 kW/m^2 (corresponding to almost 70% in the predicted W_{net}/A) if the HEPD is ignored. This arises as a consequence of variations in the: (1) net power output; and (2) heat transfer areas. The influence of the HEPD on W_{net} has been examined above, so here we turn our attention to the variations in the heat transfer areas, which are considered in more detail in Fig. 7.

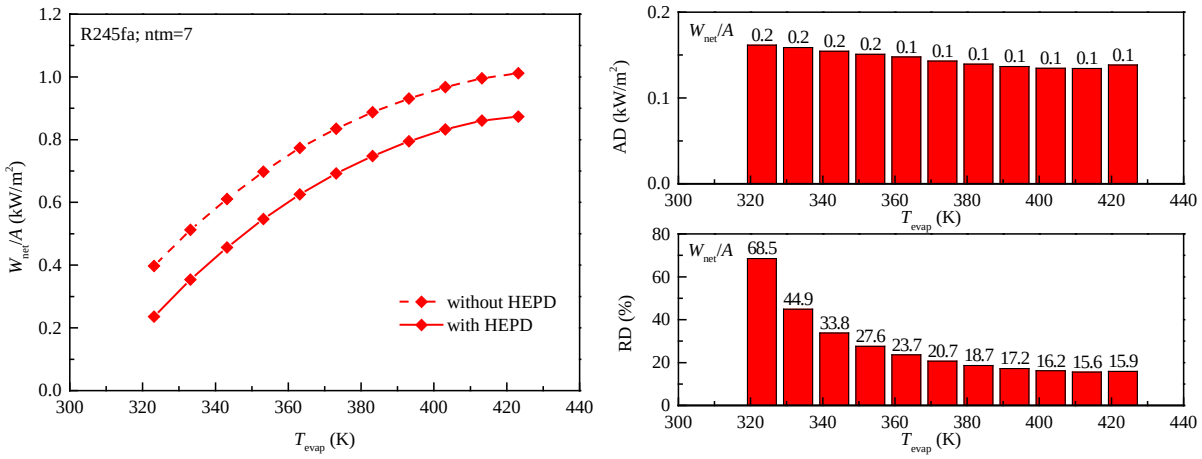

(a) Variations of W_{net}/A with T_{evap}. (b) Differences in W_{net}/A.

Figure 6. Net power output per unit heat transfer area at different evaporation temperatures.

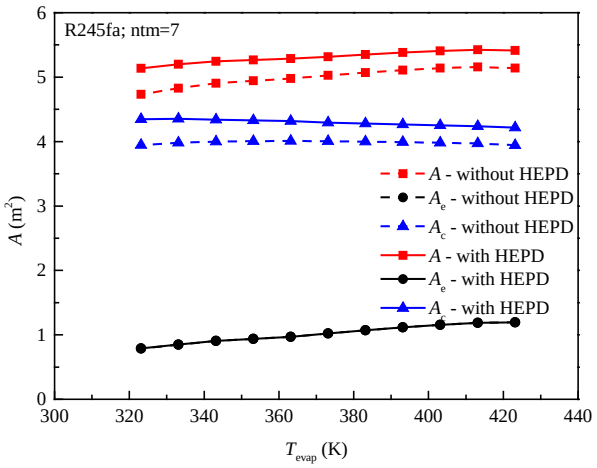

Figure 7. Heat transfer areas in the ORC system at different evaporation temperatures.

From Fig. 7 it is observed that the heat transfer area of the evaporator (A_e) remains almost the same because the state parameters related to the evaporator (i.e., temperature and pressure at the inlet and outlet) vary slightly even though the HEPD is accounted for. Nonetheless, with the HEPD, the total heat capacity of the condenser (Q_c) increases. At the same time, the heat transfer coefficients in the condenser (K_c), and especially in the de-superheating zone, reduce, due to the increased average pressure of the de-superheater that increases the density of the working fluid, and thereby lowers its velocity. According to Eq. (14), the condenser requires more heat transfer area to meet the increased heat rejection demand. Therefore, the heat transfer area of the condenser (A_c) and the total heat exchanger area of the system (A) are larger when the HEPD is fully

considered. The reduction of W_{net} and the increase of A simultaneously aggravate the economic performance of the ORC system as expressed through the parameter W_{net}/A.

3.2. ORC system design

In order to examine the influence of the HEPD on ORC system design, especially in space-constrained engine applications, heat exchangers with the same overall pattern yet different cross-sections are studied. In the present work, the cross-sections are represented by the tube numbers, and specifically the tube numbers in the midline (ntm). The cross-sections of the heat exchangers feature triangular tube layout patterns with (unit/triangle) areas limited to 0.03 m^2 [59]. Figure 8 shows cross-sectional views of the heat exchanger designs investigated in this paper, with shell diameters (D_s) of 55.5 mm, 86.8 mm, 118 mm, 150 mm and 181 mm from left to right. The results with R245fa and R600 are considered representative of HFCs and alkanes, respectively.

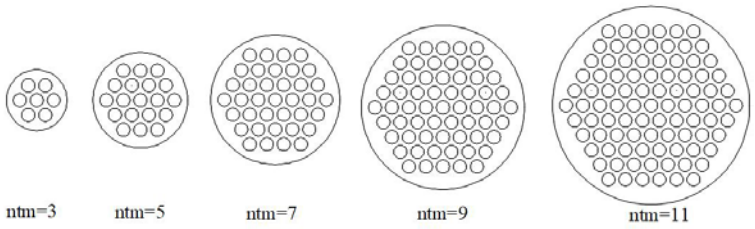

Figure 8. Cross-sectional views of the heat exchangers considered in the present study.

The resulting net power output (W_{net}) when using different heat exchanger cross-sections is shown in Fig. 9. It can be seen that W_{net} decreases when the HEPD is included, as discussed in Section 3.1. As the ntm is reduced, W_{net} decreases gradually at first and then more sharply as the ntm reduces below 7 for both R245fa and R600. The results relating to the ORC system with the smallest heat exchanger cross-section design (ntm = 3) are excluded here because the performance collapses due to the largest pressure drop in the heat exchangers. With the decrease in the shell diameter, the number of allowed tubes in the limited space also reduces. Therefore, the cross-sections on both the tube side and the shell side become smaller, which gives rise to higher mass fluxes and higher pressure drops, but also lower net power outputs.

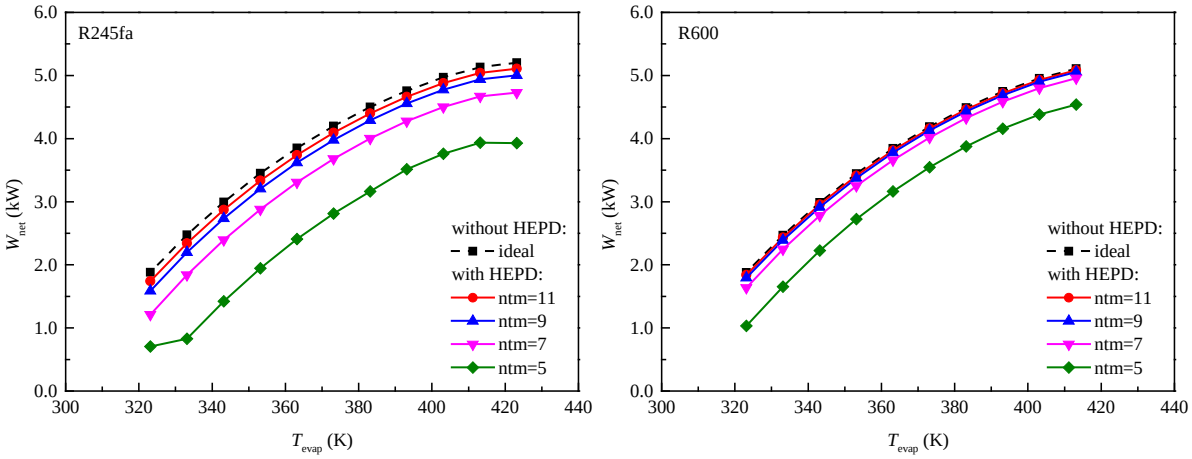

(a) R245fa. (b) R600.

Figure 9. Variations of ORC system net power output with different heat exchanger cross-sections.

Let us consider the case with T_{evap} = 403 K as an example, for which the change (with and without HEPD) in the ORC cycle on a *T*-*s* diagram is shown in Fig. 10. In this figure, the dashed lines represent the cycle calculated without the HEPD iteration, and the solid lines the improved model with the HEPD. The cycle shifts from States 1-2-3-4-5-6-1 to States 1'-2'-3'-4'-5'-6'-1'. As the diagrams suggest, in the ORC system, State 5' deviates from the ideal State 5 more markedly at ntm = 5, which greatly reduces the enthalpy drop in the expander. It is interesting to note that the cycle in this *T*-*s* diagram shifts less for R600 than it does for R245fa. W_{net} from the ORC system when using R245fa decreases from the ideal value of 4.97 kW to 3.76 kW, while W_{net} when using R600 decreases from the ideal 4.95 kW to 4.38 kW as the ntm decreases from 11 to 5, respectively. The reason for this arises from the fact that R600 can achieve the same enthalpy rise with a lower mass flow rate than R245fa, due to its higher specific heat capacity and greater enthalpy change during evaporation. Therefore, with the same heat exchanger design, the pressure drop in the heat exchangers will be lower with R600.

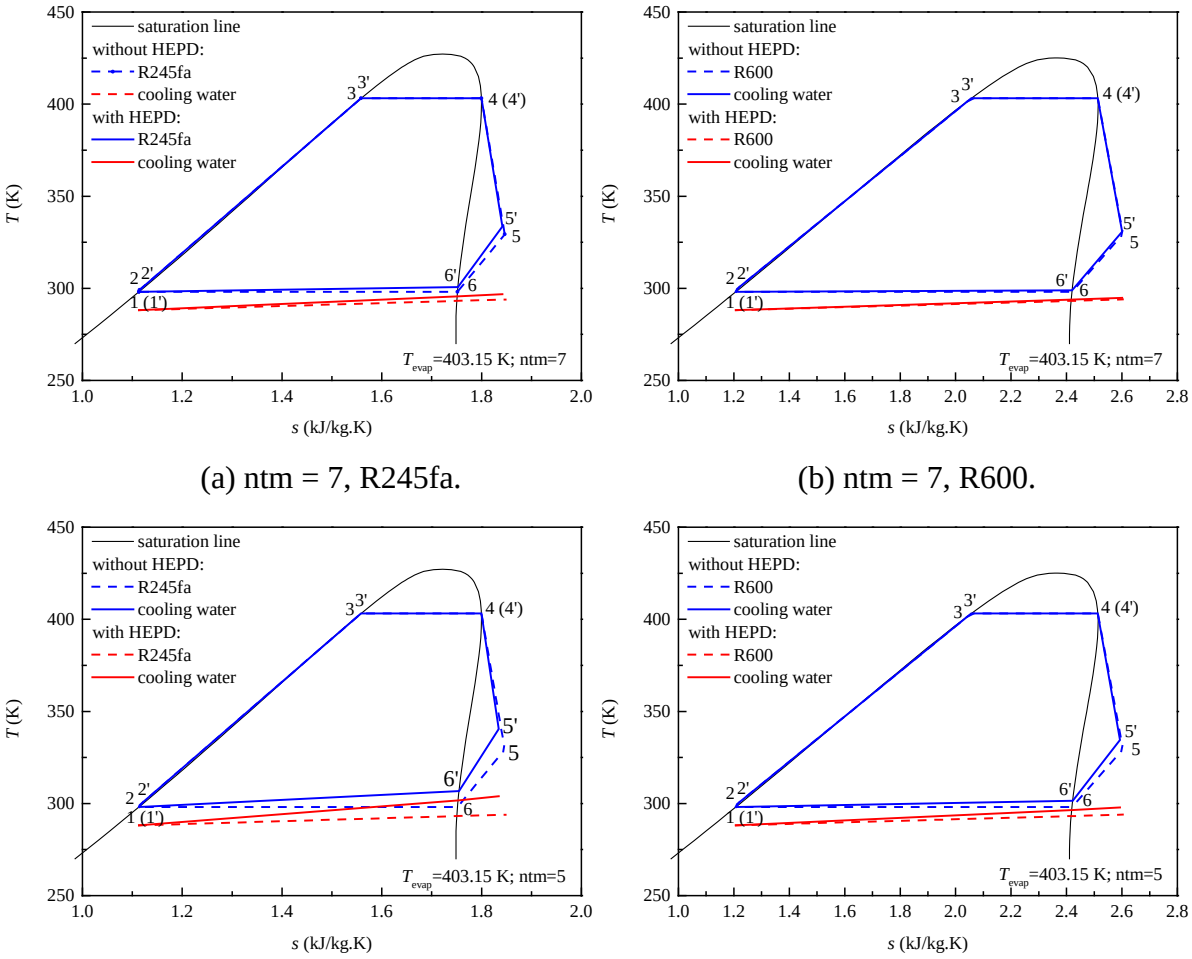

(a) ntm = 7, R245fa. (b) ntm = 7, R600.

(c) ntm = 5, R245fa. (d) ntm = 5, R600.

Figure 10. ORC thermodynamic cycle (*T*-*s* diagram) variations in response to HEPDs.

The net power output from the ORC system per unit total heat transfer area (W_{net}/A) with different heat exchanger cross-sections is explored in Fig. 11. Larger heat exchanger cross-sections worsen the economic performance of the ORC system as a result of the reduced heat transfer coefficients that arise in this case, since the velocity of the working fluid decreases in larger cross-sections. This can also be seen more directly in Fig. 12, where heat exchangers with larger ntm values require larger heat transfer areas with larger cross-sections, so smaller heat exchanger cross-sections are preferable from thermal performance and economic perspectives.

Furthermore, from Fig. 11 it appears that W_{net}/A is overestimated if the HEPD is not taken into account. The HEPD decreases the economic performance of the ORC system, and reduces the economic advantages brought by smaller heat exchangers cross-sections, especially for smaller

systems. For example, at T_{evap} = 373 K and ntm = 7, W_{net}/A is overestimated by 22%, i.e., 0.69 kW/m^2 *vs.* 0.84 kW/m^2, if the HEPDs are not involved in the performance assessment of the system with R245fa as the working fluid. These observations suggest that the HEPD should not be neglected if accurate and reliable ORC system performance evaluations are required.

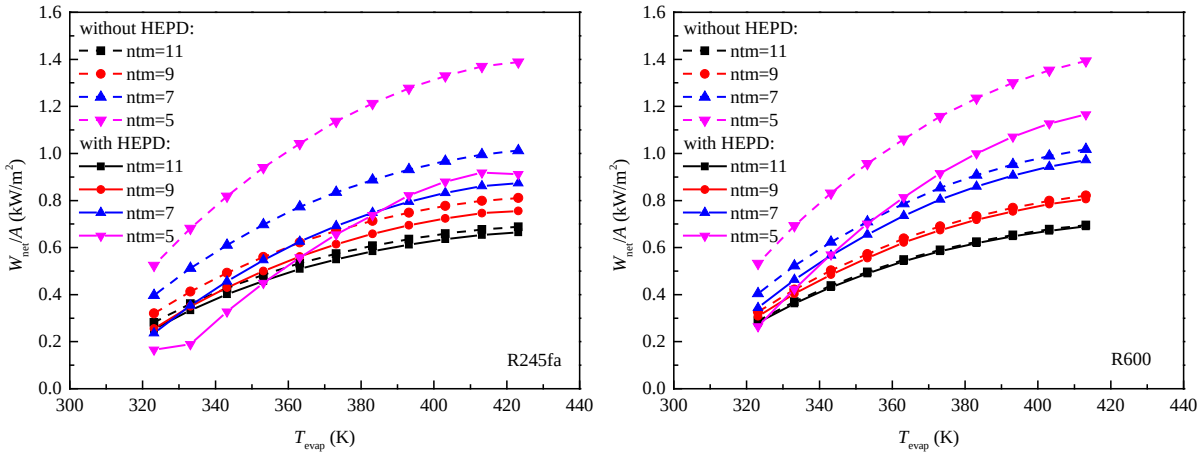

(a) R245fa. (b) R600.

Figure 11. ORC system net power output per unit heat exchanger area with different heat exchanger cross-sections.

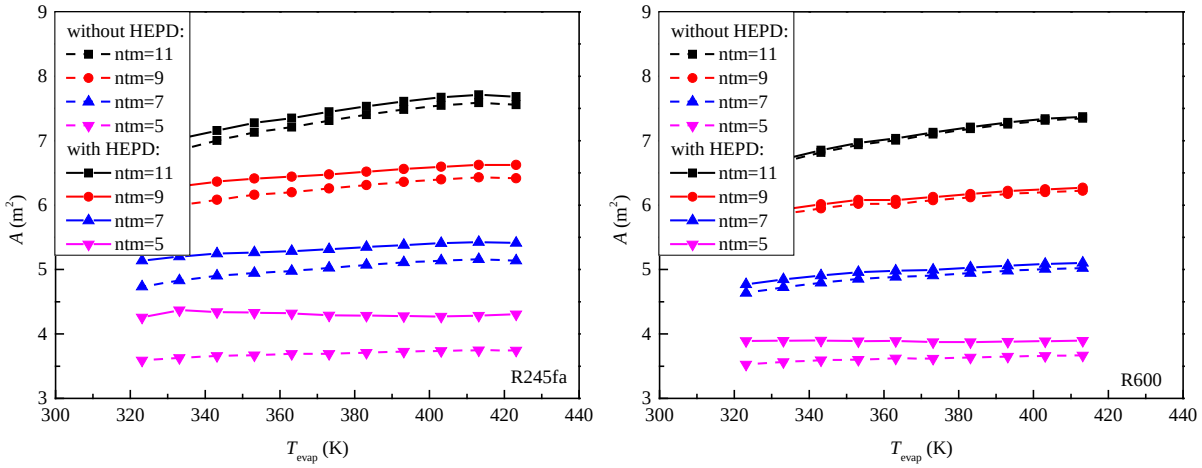

(a) R245fa. (b) R600.

Figure 12. Heat transfer area of ORC system with different heat exchanger cross-sections.

The analysis mentioned above focused on the influence of the HEPD on the design of the working-fluid side of the heat exchangers. However, the exhaust from the engine on the heat-

source side of the heat exchangers is also important, as the pressure drop on this side plays an important role in setting the ICE backpressure, which is defined as the exhaust gas pressure that is produced by the engine to overcome the hydraulic resistance of the exhaust system and to discharge the gases into the atmosphere. Increased backpressures lead to increased emissions, increased fuel consumption, and can negatively affect engine performance [59].

Figure 13 shows the pressure drop experienced by the exhaust-gas stream across the evaporator ($\Delta P_{g,e}$). It is observed that $\Delta P_{g,e}$ is affected strongly by the shell diameter but also that it does not vary considerably across the range evaporation temperatures (T_{evap}) of the working fluid. It decreases significantly with the enlargement of the heat exchanger cross-sections and also increases slightly at higher T_{evap}. High exhaust-gas pressure drops lead to an increased backpressure in the exhaust system and poorer fuel economy. Normally, larger cross-sections are preferable from an exhaust-gas pressure drop standpoint. Nonetheless, if the space of the engine application is strictly limited, a competition arises between reducing backpressure while also reducing the packaging size or volume of the heat exchanger and, by extension, of the system. If an exhaust-gas pressure drop of up to 40 kPa is allowed, these results suggest that the evaporator could be designed with an ntm of 7 for improved economic performance.

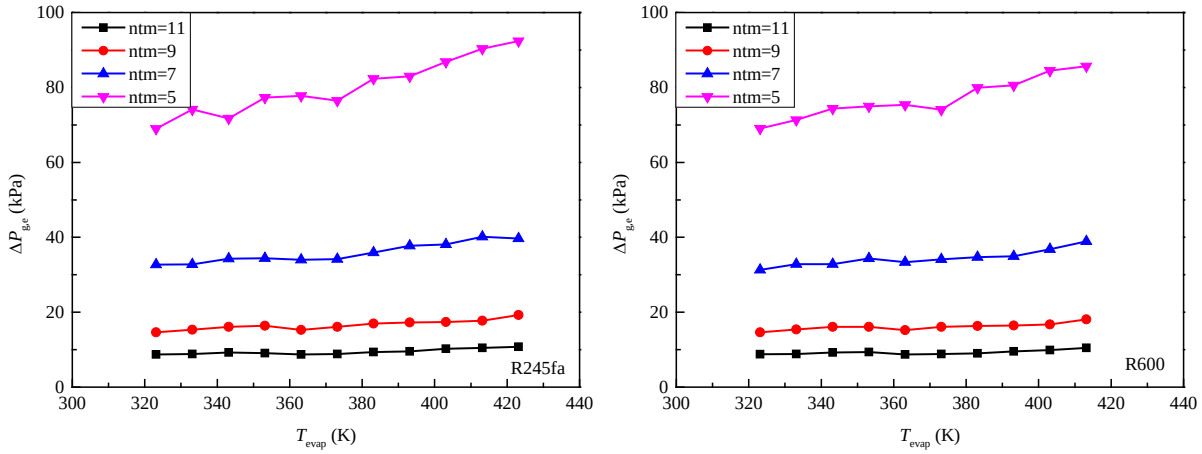

(a) R245fa. (b) R600.

Figure 13. Variations in the exhaust pressure drop with different heat exchanger cross-sections.

Table 3 provides a summary of the pros and cons related to the various heat exchanger cross-sections. '+' refers to the positive effects while '-' means the negative effects. Smaller cross-sections of the heat exchangers can enhance the heat transfer coefficient, reduce the required heat

transfer area and improve the economic performance of the ORC system. However, larger cross-section of the heat exchangers is more attractive from the pressure drop views since it will bring less deduction in the net power output of the ORC system and less influences on the original engine performance. Within the limitation of the space and the pressure drop requirement, the ORC system could employ heat exchangers with smaller cross-sections to improve its economic performance and achieve a shorter payback period.

Table 3. Trade-off summary for various heat exchanger cross-sections.

	Smaller cross-section	Larger cross-section
Heat transfer coefficient, α	+	-
Heat transfer area, A	+	-
Pressure drop of working fluid, ΔP	-	+
Net power output, W_{net}	-	+
Net power output per area, W_{net}/A	+	-
Exhaust backpressure of the engine, $\Delta P_{g,e}$	-	+

3.3. Working fluid selection

As discussed in Section 3.2, the performance of the ORC system with R245fa is affected more (relative to using R600) when accounting for the HEPD in system assessments, which indicates that the HEPD may affect the working fluid selection of the ORC system. The working fluid selection can greatly influence the ORC system performance, component sizing and costs, and also the integration with engines. Therefore, in this section, 12 organic fluids are pre-selected as candidates and the performance of corresponding ORC systems based on these fluids is evaluated by using our approach for ORC thermo-economic analysis including the HEPD. These 12 working fluids are screened based on the following criteria and Table 4 gives their properties:

1) only dry working fluids, where the inverse of slope of the saturated vapour curve is positive, are considered in this paper;

2) to avoid chemical decomposition, fluids with high critical temperatures/pressures are preferable since the ORC system is targeted for high-temperature exhaust energy recovery from engines;

3) fluids with normal boiling points near or lower than the ambient temperature enable condensation near or above atmospheric pressure, hence they are much more attractive and will

not cause a vacuum in the condenser (here, fluids with normal boiling temperatures less than or roughly around 298 K are selected); and,

4) fluids should have good environment characteristics, which can be ensured by considering their global warming potential (GWP) and ozone depletion potential (ODP).

Table 4. Working fluid properties (sorted by critical temperature from highest to lowest) [17,26].

	M_r (kg/kmol)	$T_{boiling}$ (K)	T_{crit} (K)	P_{crit} (kPa)	GWP	ODP
R245ca	134.1	298.4	447.6	3940.7	693	0
R1233zd	130.5	291.5	438.8	3570.9	1	0
R245fa	134.1	288.3	427.2	3651.0	950	0
R600	58.1	272.7	425.1	3796.0	~20	0
R236ea	152.0	279.3	412.4	3420.0	1350	0
R142b	100.5	264.0	410.3	4055.0	2310	0.12
R600a	58.1	261.4	407.8	3629.0	~20	0
R236fa	152.0	271.7	398.1	3200.0	9400	0
R124	136.5	261.2	395.4	3624.3	609	0.02
R1234ze	114.0	254.2	382.5	3634.9	<1	0
R227ea	170.0	256.8	374.9	2925.0	3220	0
R1234yf	114.0	243.7	367.9	3382.2	<1	0

Figure 14 shows how the net power output (W_{net}) of the ORC system varies with the choice of the working fluid. When not accounting for the HEPD, R245ca is associated with the greatest net power output, followed by R1234zd, R245fa and butane (R600). This is strongly linked to the differences in their critical temperatures. For the high-temperature exhaust used here as the heat source, working fluids with higher critical temperatures can be heated to higher pressures and temperatures, leading to better thermal efficiency and power output. When accounting for the HEPD, W_{net} decreases slightly for all the working fluids if ntm is greater than 9, with maximum relative differences in W_{net} of around 5%.

However, W_{net} shows a more considerable reduction when the ntm is less than 9. If we take ntm = 7 as an example, W_{net} is reduced by 13%, from 5.63 kW to 4.88 kW, in the ORC system with R245ca, while only marginally decreasing by 3%, from 5.11 kW to 4.96 kW, in the ORC system with

R600. This has very important implications as it indicates that R600 could outperform R245ca in a real application, even though the ideal net power output from an ORC system with R245ca is higher than that with R600 in theoretical calculations. Moreover, there is a sharp drop in W_{net} when the shell diameter is substantially decreased to 86.8 mm (ntm = 5), affecting the previous selection sequence for the preferred working fluid amongst the 12 candidate fluids, based on W_{net}. With the exception of R142b and R600a, the overestimation of W_{net} when not accounting for the HEPD is significant and amounts to >10% for all other investigated fluids, with R245ca, R1233zd and R245fa having the largest overestimations of 49%, 40% and 32%, respectively.

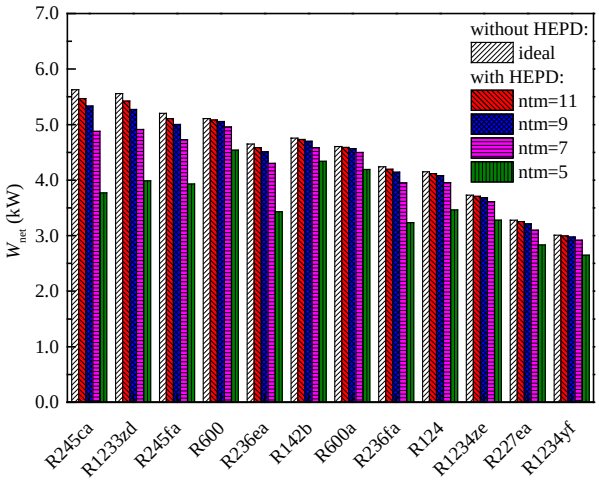

Figure 14. Net power output of the ORC system with different working fluids.

Figure 15 compares the net power output per unit heat transfer area (W_{net}/A) of the ORC system when using different heat exchanger designs. As an overall trend, W_{net}/A shows different levels of reduction for each working fluid when the HEPD is included. Without the HEPD, R245ca ranks as the best fluid from the perspective of the highest W_{net}/A, irrespective of which type of heat exchanger design is chosen. However, R142b outperforms R245ca if the heat exchangers are designed to have 11 tubes in the midline, while R600 has the highest value of W_{net}/A if ntm is chosen to be 9 in the heat exchanger. A look at the four sub-plots reveals that W_{net}/A has a similar variation to that of W_{net} when comparing different heat exchanger designs, but the relative differences between performance estimates with and without the HEPD are larger when predicting W_{net}/A compared to W_{net}, which is important as it implies that it is even more important to account for the HEPD when performing economic analyses. For example, in the ORC system with R245ca

and ntm = 9 in the heat exchanger design, the relative difference of W_{net}/A is as almost twice as that of W_{net} (12.8% vs. 5.5%), showing a greater overestimation of economic performance evaluation without the HEPD. The largest overestimation between predictions without the HEPD of slightly over 80% (specifically, 82%) can be seen for ntm = 5 and R245ca. In other cases, the overestimation is smaller, but still significant, e.g., by up to 65% with R1233zd, 52% with R245fa, and 55% with R236ea.

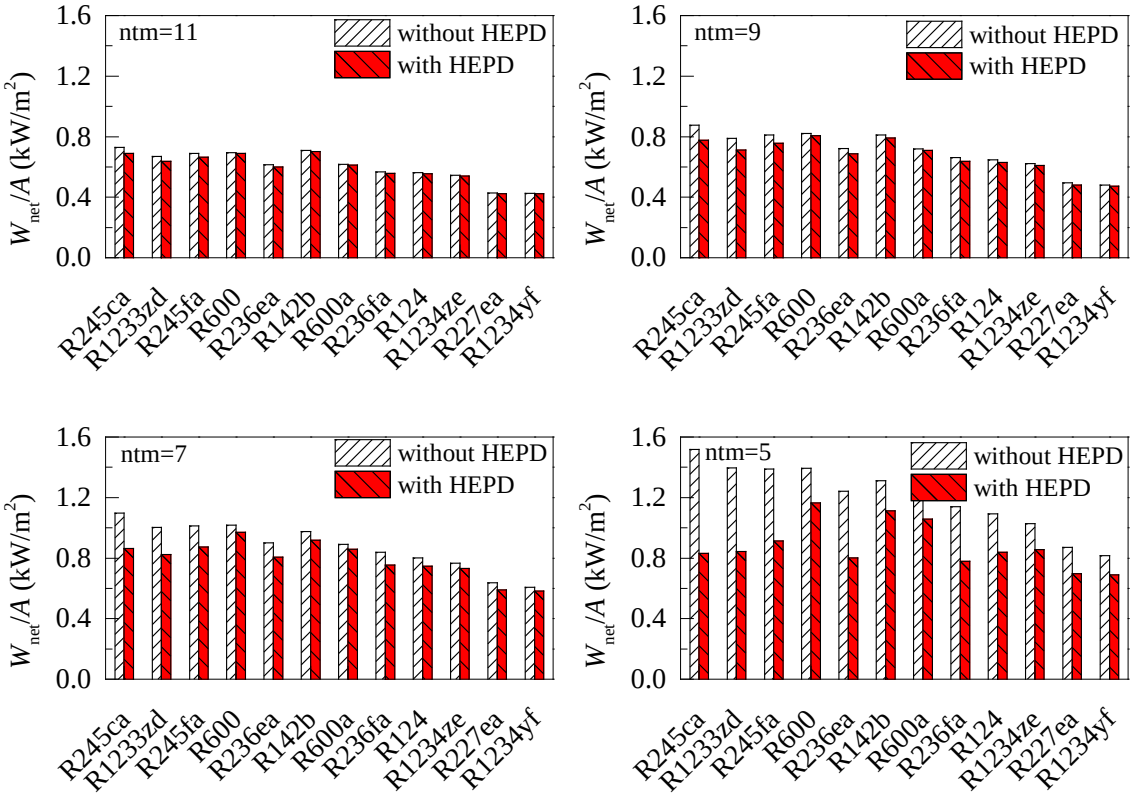

Figure 15. Net power output per unit heat transfer area with different working fluids.

Table 5 lists the best working fluids (top 3) from thermo-economic analyses with the conventional method (ignoring the HEPD) and the improved approach (involving the HEPD). As mentioned earlier, for heat exchangers with a smaller shell diameter, the HEPD will affect the working fluid performance (and selection). For both cases when ntm is 11, ranking by W_{net} from the largest to the smallest, R245ca is the best, followed by R1233zd and R245fa. Ranking by W_{net}/A, the first three are R245ca, R142b and R600 without the HEPD, which changes to R142b, R600

and R245ca with the HEPD. If ntm is less than 9, the optimal working fluid changes from R245ca to R600 from both a thermodynamic performance and economic viability perspective.

Table 5. Working fluid selection comparisons with conventional and revised approaches.

		Without HEPD			With HEPD		
Design	Index	Rank 1st	Rank 2nd	Rank 3rd	Rank 1st	Rank 2nd	Rank 3rd
ntm = 11	W_{net}	R245ca	R1233zd	R245fa	R245ca	R1233zd	R245fa
	W_{net}/A	R245ca	R142b	R600	R142b	R600	R245ca
ntm = 9	W_{net}	R245ca	R1233zd	R245fa	R245ca	R1233zd	R600
	W_{net}/A	R245ca	R600	R142b	R600	R142b	R245ca
ntm = 7	W_{net}	R245ca	R1233zd	R245fa	R600	R1233zd	R245ca
	W_{net}/A	R245ca	R600	R245fa	R600	R142b	R245fa
ntm = 5	W_{net}	R245ca	R1233zd	R245fa	R600	R142b	R600a
	W_{net}/A	R245ca	R1233zd	R600	R600	R142b	R600a

4. Further economic considerations

Section 3 has presented data, along with an associated discussion, that relate to a comparison between conventional methods and the improved approach for ORC system analysis presented in this work (including the HEPD). In this section, variations of the specific investment cost (SIC) and the and the depreciated payback period (DPP) and the effects of other cycle parameters (e.g., exhaust conditions, condensation temperatures) are briefly discussed.

4.1. Costs and payback

To have a better understanding of the economic performance of the ORC system, the influence of the HEPD on the specific investment cost (SIC) and depreciated payback period (DPP) are demonstrated in Fig. 16. The results are depicted for the heat exchangers with ntm = 7 and for each working fluid at the optimal evaporation temperature in terms of the maximum W_{net}. With the consideration of HEPD, both the SIC and the DPP are higher, implying an underestimation if the HEPD is not included in performance analysis. If we take R245fa as an example, the SIC is underestimated as 20.4 $/W while it should be 22.0 $/W. The DPP is underestimated as 15.6 years while it should be 17.9 years. The reason is that the consideration of the HEPD leads to larger heat transfer areas for the heat

exchangers and additional power consumption of the pump, which would bring higher purchasing costs based on the cost estimation equations as listed in Table 1. Hence, the ORC system costs when considering the HEPD are higher. At the same time, the HEPD also deteriorates the net power output of the ORC systems as shown in Fig. 4. For the ORC systems with R1234yf as the working fluid, the SIC is underestimated from 42.3 $/W to 41.0 $/W. It should be noted that the DPP is not shown in Fig. 16 because of the negative value, which means the ORC systems with R1234yf is not profitable with the assumption of yearly full-load operation of 7500 h, the electricity price of 0.3 $/kWh and the discount rate of 5%. With a lower discount rate (say 2%) or higher on-grid electricity price (say 0.5 $/kWh), the use of R1234yf could be beneficial.

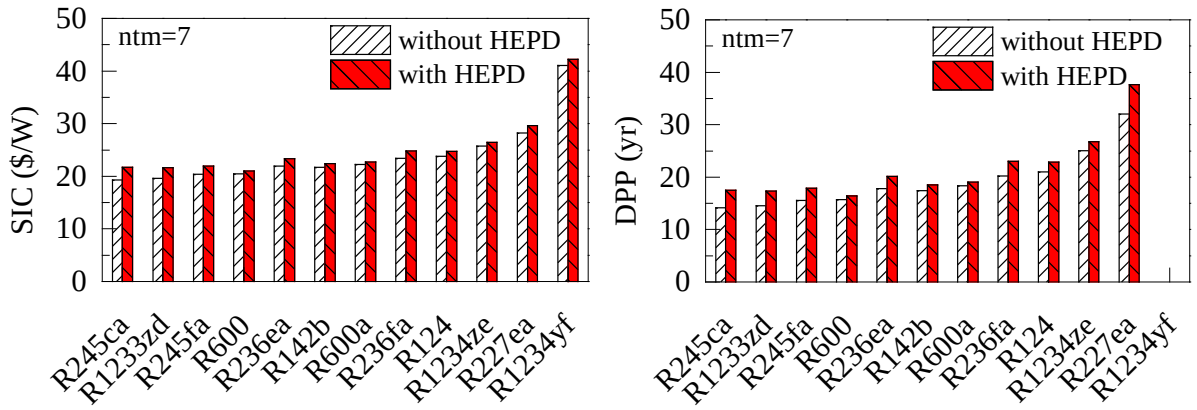

Figure 16. Specific investment cost (SIC) and depreciated payback period (DPP) with different working fluids.

4.2. Heat source conditions

The heat source conditions are represented by the flow rate and temperature of the exhaust gases. Here, the evaporation and condensation temperatures are fixed to 403 K and 298 K, respectively. Therefore, the flow rate of the working fluid in the ORC system will be directly influenced by the changes in the heat source conditions. Table 6 gives the main results for the ORC system with R245fa as the working fluid, when the exhaust temperature varies from 573 K to 873 K. A consideration of the HEPD results in greater variations in both W_{net} and W_{net}/A at higher exhaust temperatures due to the larger flow rate of the working fluid, indicating that the HEPD should be taken into account especially adopting the heat sources of high temperature and large mass flow rate.

Table 6. ORC system performance variations with R245fa at different exhaust temperatures.

$T_{g,in}$ (K)	W_{net} (kW)		RD (%)	W_{net}/A (kW/m^2)		RD (%)
	With HEPD	Without HEPD		With HEPD	Without HEPD	
573	3.13	3.28	4.79	0.70	0.76	8.57
623	3.91	4.22	7.93	0.78	0.87	11.54
673	4.64	5.16	11.21	0.84	0.99	17.86
723	5.32	6.12	15.04	0.89	1.10	23.60
773	5.82	7.09	21.82	0.89	1.20	34.83
823	6.49	8.08	24.50	0.94	1.29	37.23
873	6.97	9.08	30.27	0.93	1.37	47.31

4.3. Condensation temperature

In the aforementioned results, the condensation temperature (T_{cond}) was fixed to 298 K. Here, we vary T_{cond} from 298 K to 318 K in 5 K intervals, with R245fa and T_{evap} fixed to 403 K. Table 7 presents the main results. As T_{cond} increase the relative differences (in the predicted indicators with and without HEPD) in both W_{net} and W_{net}/A reduce, as a consequence of smaller pressure drops. It is clear that the de-superheating section becomes smaller and the average velocity in the tubes decreases due to increased condensation pressure. These findings indicate that it is particularly important to consider the HEPD at lower condensation temperatures.

Table 7. ORC system performance variations with R245fa at different condensation temperatures.

T_{cond} (K)	W_{net} (kW)		RD (%)	W_{net}/A (kW/m^2)		RD (%)
	With HEPD	Without HEPD		With HEPD	Without HEPD	
298	4.50	4.97	10.44	0.83	0.97	16.87
303	4.38	4.74	8.22	0.88	0.98	11.36
308	4.22	4.51	6.87	0.89	0.97	8.99
313	4.06	4.29	5.67	0.89	0.95	6.74
318	3.88	4.06	4.64	0.87	0.92	5.75

5. Conclusions

ORC systems have been widely studied in the context of waste heat recovery. In conventional ORC system assessments, the heat exchanger pressure drops (HEPDs) are normally ignored. However, the pressure drops can detrimentally affect the ORC system performance, especially in space-constrained applications where it is necessary to restrict the heat exchanger (and system) size while tolerating higher pressure drops. In this paper, thermo-economic analyses have been conducted by integrating calculations of the HEPDs in both heat exchangers of a subcritical non-recuperative ORC system into ORC system modelling. The proposed approach improves the reliability and accuracy of ORC system assessments, making these more representative of practical implementations.

Some of the more important conclusions from the present work are listed below.

(1) Both the thermodynamic performance (in terms of the net power output) and the economic performance (in terms of the net power output per unit heat transfer area) of ORC systems are overestimated without the consideration of the HEPD, especially at lower evaporation or condensation temperatures for a given heat-source temperature, and also for high-temperature heat sources. This makes the results particularly relevant to ORC applications relating to waste-heat recovery and conversion from the exhaust gases of internal combustion engine and other similar (e.g., biomass/gas) high-temperature heat sources. In particular, economic indicators were shown be overestimated by up to 82% in some cases (e.g., see Fig. 15 for a small number of tubes in the heat exchanger, and with R245ca). In other cases, the overestimation is smaller, but still significant, e.g., by up to 65% with R1233zd, 52% with R245fa, and 55% with R236ea.

(2) The conflicts between space, pressure drop, net power output, heat exchanger area requirements and system costs which arise in space-constrained engine, especially mobile applications, are nontrivial. Given restrictions on the allowable exhaust gas backpressure, the heat exchangers can be designed with smaller cross-sections to reduce packaging volume, enhance heat transfer and improve system economy while maintaining a high power output.

(3) The optimal working fluid changes if HEPD is considered since different working fluids experience different pressure drops in the heat exchangers, and especially in the condenser. In the cases investigated in this work, the best working fluid changes from R245ca to R142b or R600 depending on the heat exchanger design. It is therefore also concluded that HEPDs should be taken into account in working fluid selection to avoid departures between theory and practice.

Acknowledgements

This work was supported by National Key R&D Program of China (2018YFB01059000). The authors would also like to thank the UK Engineering and Physical Sciences Research Council [grant number EP/P004709/1] and the China Scholarship Council for a joint-PhD scholarship that supported Xiaoya Li for this research. Data supporting this publication can be obtained on request from cep-lab@imperial.ac.uk.

References

[1] Fu J., Liu J., Feng R., Yang Y., Wang L., Wang Y., Energy and exergy analysis on gasoline engine based on mapping characteristics experiment. Applied Energy 2013;102:622-630.

[2] Shu G., Zhao M., Tian H., Huo Y., Zhu W., Experimental comparison of R123 and R245fa as working fluids for waste heat recovery from heavy-duty diesel engine. Energy 2016;115:756-769.

[3] Sprouse C., Depcik C., Review of organic Rankine cycles for internal combustion engine exhaust waste heat recovery. Applied Thermal Engineering 2013;51(1):711-722.

[4] Markides C.N., The role of pumped and waste heat technologies in a high-efficiency sustainable energy future for the UK. Applied Thermal Engineering 2013;53(2):197-209.

[5] Liang Y., Bian X., Qian W., Pan M., Ban Z., Yu Z., Theoretical analysis of a regenerative supercritical carbon dioxide Brayton cycle/organic Rankine cycle dual loop for waste heat recovery of a diesel/natural gas dual-fuel engine. Energy Conversion and Management 2019;197:111845.

[6] Mahmoudi A., Fazli M., Morad M.R., A recent review of waste heat recovery by Organic Rankine Cycle. Applied Thermal Engineering 2018;143:660-675.

[7] Markides C.N., Low concentration solar-power systems based on organic Rankine cycles for distributed-scale applications: overview and further developments. Frontiers in Energy Research 2015;3:47.

[8] Nami H., Ertesvåg I.S., Agromayor R., Riboldi L., Nord L.O., Gas turbine exhaust gas heat recovery by organic Rankine cycles (ORC) for offshore combined heat and power applications - Energy and exergy analysis. Energy 2018;165:1060-1071.

[9] Shi L., Shu G., Tian H., Deng S., A review of modified Organic Rankine cycles (ORCs) for internal combustion engine waste heat recovery (ICE-WHR). Renewable and Sustainable Energy Reviews 2018;92:85-110.

[10] Xu B., Rathod D., Yebi A., Filipi Z., Onori S., Hoffman M., A comprehensive review of organic rankine cycle waste heat recovery systems in heavy-duty diesel engine applications. Renewable and Sustainable Energy Reviews 2019;107:145-170.

[11] Chen T., Zhuge W., Zhang Y., Zhang L., A novel cascade organic Rankine cycle (ORC) system for waste heat recovery of truck diesel engines. Energy Conversion and Management 2017;138:210-223.

[12] Liang Y., Shu G., Tian H., Wei H., Liang X., Liu L., Wang X., Theoretical analysis of a novel electricity–cooling cogeneration system (ECCS) based on cascade use of waste heat of marine engine. Energy Conversion and Management 2014;85:888-894.

[13] Song J., Song Y., Gu C., Thermodynamic analysis and performance optimization of an organic Rankine cycle (ORC) waste heat recovery system for marine diesel engines. Energy 2015;82:976-985.

[14] Tian H., Chang L., Shu G., Shi L., Multi-objective optimization of the carbon dioxide transcritical power cycle with various configurations for engine waste heat recovery. Energy Conversion and Management 2017;148:477-488.

[15] Chatzopoulou M.A., Markides C.N., Thermodynamic optimisation of a high-electrical efficiency integrated internal combustion engine – organic Rankine cycle combined heat and power system. Applied Energy 2018;226:1229-1251.

[16] Chatzopoulou M.A., Simpson M., Sapin P., Markides C.N., Off-design optimization of organic Rankine cycle (ORC) engines with piston expanders for medium-scale combined heat and power applications. Applied Energy 2019;238:1211-1236.

[17] Tian H., Shu G., Wei H., Liang X., Liu L., Fluids and parameters optimization for the organic Rankine cycles (ORCs) used in exhaust heat recovery of internal combustion engine (ICE). Energy 2012;47:125-136.

[18] Wang E., Zhang H., Fan B., Ouyang M., Zhao Y., Mu Q., Study of working fluid selection of organic Rankine cycle (ORC) for engine waste heat recovery. Energy 2011;36(5):3406-3418.

[19] Oyewunmi O.A., Kirmse C.J., Panteleo A.M., Markides C.N., Performance of working-fluid mixtures in ORC-CHP systems for different heat-demand segments and heat-recovery temperature levels. Energy Conversion and Management 2017;148:1508-1524.

[20] Song J., Gu C., Analysis of ORC (organic Rankine cycle) systems with pure hydrocarbons and mixtures of hydrocarbon and retardant for engine waste heat recovery. Applied Thermal Engineering 2015;89:693-702.

[21] Oyewunmi O.A., Taleb A.I., Haslam A.J., Markides C.N., On the use of SAFT-VR Mie for assessing large-glide fluorocarbon working-fluid mixtures in organic Rankine cycles. Applied Energy 2016;163:263-282.

[22] Su W., Zhao L., Deng S., Developing a performance evaluation model of Organic Rankine Cycle for working fluids based on the group contribution method. Energy Conversion and Management 2017;132:307-315.

[23] White M.T., Oyewunmi O.A., Chatzopoulou M.A., Pantaleo A.M., Haslam A.J., Markides C.N., Computer-aided working-fluid design, thermodynamic optimisation and thermoeconomic assessment of ORC systems for waste-heat recovery. Energy 2018;161:1181-1198.

[24] White M.T., Oyewunmi O.A., Haslam A.J., Markides C.N., Industrial waste-heat recovery through integrated computer-aided working-fluid and ORC system optimisation using SAFT-γ Mie. Energy Conversion and Management 2017;150:851-869.

[25] van Kleef L.M.T., Oyewunmi O.A., Markides C.N., Multi-objective thermo-economic optimization of organic Rankine cycle (ORC) power systems in waste-heat recovery applications using computer-aided molecular design techniques. Applied Energy 2019;251:112513.

[26] Song J., Gu C., Ren X., Influence of the radial-inflow turbine efficiency prediction on the design and analysis of the organic Rankine cycle (ORC) system. Energy Conversion and Management 2016;123:308-316.

[27] Mounier V., Olmedo L.E., Schiffmann J., Small scale radial inflow turbine performance and pre-design maps for Organic Rankine Cycles. Energy 2018;143:1072-1084.

[28] Sapin P., Simpson M., White A.J., Markides C.N., Lumped dynamic analysis and design of a high-performance reciprocating-piston expander. 30th International Conference on

Efficiency, Cost, Optimization, Simulation and Environmental Impact of Energy Systems (ECOS), 2017.

[29] Simpson M., Rotolo G., Sapin P., De Palma P., White A.J., Markides C.N., Thermodynamic performance maps of reciprocating-piston expanders for operation at off-design and part-load conditions, 13th International Conference on Heat Transfer, Fluid Mechanics and Thermodynamics (HEFAT), 2017.

[30] Bianchi M., Branchini L., Casari N., De Pascale A., Melino F., Ottaviano S., Pinelli M., Spina P.R., Suman A., Experimental analysis of a micro-ORC driven by piston expander for low-grade heat recovery. Applied Thermal Engineering 2019;148:1278-1291.

[31] Zhang Y., Wu Y., Xia G., Ma C., Ji W., Liu S., et al., Development and experimental study on organic Rankine cycle system with single-screw expander for waste heat recovery from exhaust of diesel engine. Energy 2014;77:499-508.

[32] Ziviani D., Gusev S., Lecompte S., Groll E.A., Braun J.E., Horton W.T., et al., Characterizing the performance of a single-screw expander in a small-scale organic Rankine cycle for waste heat recovery. Applied Energy 2016;181:155-170.

[33] Nikolov A., Brümmer A., Investigating a small oil-flooded twin-screw expander for waste-heat utilisation in organic Rankine cycle systems. Energies 2017;10(7),869.

[34] Yan J., Han Y., Tian J., Xu Y., Zhang Y., Chen R., Performance investigation of a novel expander coupling organic Rankine cycle: Variable expansion ratio rotary vane expander for variable working conditions. Applied Thermal Engineering 2019;152:573-581.

[35] Ibarra M., Rovira A., Alarcón-Padilla D., Performance of an Organic Rankine Cycle with two expanders at off-design operation. Applied Thermal Engineering 2019;149:688-701.

[36] Zhao M., Canova M., Tian H., Shu G., Design space exploration for waste heat recovery system in automotive application under driving cycle. Energy 2019;176:980-990.

[37] Hatami M., Jafaryar M., Ganji D.D., Gorji-Bandpy M., Optimization of finned-tube heat exchangers for diesel exhaust waste heat recovery using CFD and CCD techniques. International Communications in Heat and Mass Transfer 2014;57:254-263.

[38] Mastrullo R., Mauro A.W., Revellin R., Viscito L., Modeling and optimization of a shell and louvered fin mini-tubes heat exchanger in an ORC powered by an internal combustion engine. Energy Conversion and Management 2015;101:697-712.

[39] Mokkapati V., Lin C., Numerical study of an exhaust heat recovery system using corrugated tube heat exchanger with twisted tape inserts. International Communications in Heat and Mass Transfer 2014;57:53-64.

[40] Chen T., Shu G., Tian H., Ma X., Wang Y., Yang H., Compact potential of exhaust heat exchangers for engine waste heat recovery using metal foams. International Journal of Energy Research 2019;43:1428-1443.

[41] Nematollahi O., Abadi G.B., Kim D.Y., Kim K.C., Experimental study of the effect of brazed compact metal-foam evaporator in an organic Rankine cycle performance: Toward a compact ORC. Energy Conversion and Management 2018;173:37-45.

[42] Lakhani S., Raul A., Saha S.K., Dynamic modelling of ORC-based solar thermal power plant integrated with multitube shell and tube latent heat thermal storage system. Applied Thermal Engineering 2017;123:458-470.

[43] Horst T.A., Rottengruber H., Seifert M., Ringler J., Dynamic heat exchanger model for performance prediction and control system design of automotive waste heat recovery systems. Applied Energy 2013;105:293-303.

[44] Feru E., Jager B., Willems F., Steinbuch M., Two-phase plate-fin heat exchanger modeling for waste heat recovery systems in diesel engines. Applied Energy 2014;133:183-196.

[45] Shu G., Li X., Tian H., Shi L., Wang X., Yu G., Design condition and operating strategy analysis of CO_2 transcritical waste heat recovery system for engine with variable operating conditions. Energy Conversion and Management 2017;142:188-199.

[46] Yu G., Shu G., Tian H.., Wei H, Liang X., Multi-approach evaluations of a cascade-organic Rankine cycle (C-ORC) system driven by diesel engine waste heat: Part B-techno-economic evaluations. Energy Conversion and Management 2016;108:596-608.

[47] Galindo J., Climent H., Dolz V., Royo-Pascual L., Multi-objective optimization of a bottoming organic Rankine cycle (ORC) of gasoline engine using swash-plate expander. Energy Conversion and Management 2016;126:1054-1065.

[48] Yang F., Zhang H., Bei C., Song S., Wang E., Parametric optimization and performance analysis of ORC (organic Rankine cycle) for diesel engine waste heat recovery with a fin-and-tube evaporator. Energy 2015;91:128-141.

[49] Yang M., Yeh R., Thermodynamic and economic performances optimization of an organic Rankine cycle system utilizing exhaust gas of a large marine diesel engine. Applied Energy 2015;149:1-12.

[50] Xia J., Wang J., Lou J., Zhao P., Dai Y., Thermo-economic analysis and optimization of a combined cooling and power (CCP) system for engine waste heat recovery. Energy Conversion and Management 2016;128:303-316.

[51] Astolfi M., Alfani D., Lasala S., Macchi E., Comparison between ORC and CO_2 power systems for the exploitation of low-medium temperature heat sources. Energy 2018;161:1250-1261.

[52] Tian H., Chang L., Gao Y., Shu G., Zhao M., Yan N., Thermo-economic analysis of zeotropic mixtures based on siloxanes for engine waste heat recovery using a dual-loop organic Rankine cycle (DORC). Energy Conversion and Management 2017;136:11-26.

[53] Zhang C., Liu C.., Wang S., Xu X., Li Q., Thermo-economic comparison of subcritical organic Rankine cycle based on different heat exchanger configurations. Energy 2017;123:728-741.

[54] Thulukkanam K., Heat exchanger design handbook. Second Edition. CRC Press; 2013.

[55] Galindo J., Dolz V., Royo-Pascual L., Brizard A., Dynamic modeling of an organic Rankine cycle to recover waste heat for transportation vehicles. Energy Procedia 2017;129:192-199.

[56] Dobson M.K., Chato J.C., Condensation in smooth horizontal tubes. Journal of Heat Transfer 1998;120(1):193-213.

[57] Turton R., Bailie R.C., Whiting W.B., Shaeiwitz J.A., Analysis, synthesis and design of chemical processes. Third Edition. Pearson Education; 2008.

[58] Chemical Engineering Online, <https://www.chemengonline.com/cepci-updates-january-2018-prelim-and-december-2017-final/?printmode=1>, [accessed 24 May 2019].

[59] Folgueira A., Teniente J., Carballido R., A system-level approach to the development of optimized waste heat recovery exhaust evaporators. SAE Technical Paper 2018; 2018-01-1365.